Research paper

The origin of carbonate cements in the Hildasay reservoir, Cambo Field, Faroe-Shetland Basin; clumped isotopic analysis and implications for reservoir performance

Kevin Purvis [a,*], Paul Dennis [b], Liam Holt [a,1], Alina Marca [b]

[a] Siccar Point Energy Limited, H1 Hill of Rubislaw, Aberdeen, AB15 6BY, UK
[b] Stable Isotope Laboratory, School of Environmental Sciences, University of East Anglia, Norwich, NR4 7TJ, UK

ABSTRACT

The early Eocene paralic sandstones of the Hildasay Member of the Flett Formation form the major oil-bearing reservoir in the Cambo Field, located in the Faroe-Shetland Basin. The sandstones locally contain calcite-cemented intervals that vary in thickness from decimetre to over 1 m. A calcite-cemented interval from well 204/10a-5 has been analysed petrographically and using clumped isotopes to determine its mode of formation and potential lateral extent. Petrographic analysis shows the cemented interval to consist of ferroan calcite, with a consistent dull red cathodoluminescence, suggesting a single phase of precipitation. The centre of the cemented interval comprises a finer grained unit with detrital kerogen and early sphaerosiderite, while the rest comprises homogeneous porosity-occluding ferroan calcite. The early sphaerosiderite in the centre is replaced by ferroan calcite with a high δ^{13} carbon isotopic signature (δ^{13} C$_{VPDB}$ = 7.53‰) suggesting that it formed during anaerobic methanogenesis or fermentation. Samples from the intermediate zone have a lower δ^{13} carbon isotopic composition (δ^{13} C$_{VPDB}$ = 0.72 to −3.68‰). In comparison the outer margin of the cemented unit has an even lower δ^{13} carbon isotopic signature (δ^{13} C$_{VPDB}$ = −15.5 to -15.9‰) more typical of a strong aerobic oxidation source. The oxygen isotopic signature of the cements is similar (δ^{18} O$_{VPDB}$ = −10.9 to −12.2‰). Analysis of the clumped isotopes suggest that the ferroan calcite formed at ~40–50 °C, from pore waters that were predominantly meteoric in origin (δ^{18} O$_{VSMOW}$ = −4.8 to −5.7‰). Burial history modelling would suggest that the cements formed at a depth of ~500–1000 m. Meteoric water was likely to have been introduced during the formation of the mid-Lutetian unconformity ~45Mya, approximately 10 Mya after the sandstones were deposited. The model proposed is that ferroan calcite precipitation was initiated in the fine lag deposits that contained the kerogen and sphaerosiderite, and then grew outwards. If the model is correct, the cemented units should be restricted to this facies and consequently of limited lateral extent. Consequently, it is likely that the cemented intervals will have a limited impact upon the reservoir performance and are unlikely to act as major barriers to fluid flow.

1. Introduction

Calcite-cemented layers have been widely reported in shallow marine sandstone reservoirs where they sometimes have a lateral extent of several kilometres (Bryant et al. 1988; Walderhaug et al. 1989; Bjorkum and Walderhaug 1993). Similar carbonate cemented units have also been reported in deep water turbidite reservoirs (Carvalho et al. 1995; Dutton, 2008, Watson et al., 1995). In siliciclastic sequences the reservoir quality and production performance are largely influenced by the

abundance and distribution of carbonate cementation, with laterally extensive cemented units acting as flow barriers, increasing heterogeneity and having a significant impact on production and sweep efficiency where water flood techniques are utilised. Consequently, understanding the nature and distribution of carbonate cements is important for predicting reservoir performance (Carvalho et al. 1995; Dutton, 2008).

The Hildasay reservoir comprises a sequence of paralic units deposited during the early Eocene. These sandstones form the reservoir

---

interval in the Cambo Field located in the Faroe-Shetland Basin, a field that contains over 800 million barrels of oil and is currently being developed. The reservoir sandstones are typically of excellent quality (30% porosity and multi-Darcy permeability) but locally are extensively cemented, forming cemented intervals over 1 m in thickness as observed in core. Given the limited number of wells drilled to date, and the limited core taken, it is unclear as to whether these cemented units are concretions, or more laterally extensive layers. The latter scenario would have implications for oil production, and consequently this study was designed to determine if it would be possible to define the geometry of the carbonate-cemented intervals and their mode of origin. To fulfil this objective, as well as utilising standard petrographic techniques including X-Ray Diffraction (XRD), Scanning electron Microscopy (SEM), petrographic cold cathodoluminescence (CL), and standard thin section petrography, stable isotopic analysis (C and O) and clumped isotopic analysis were undertaken to evaluate the temperature and porewater isotopic composition of the fluids that the carbonate formed from.

2. Geological setting

The Cambo Field is located in UK Blocks 204/09a, 204/10a, 204/04a and 204/05a, in the Faroe-Shetland Basin (Fig. 1) and is a significant hydrocarbon resource. The field is operated by Siccar Point Energy E&P Ltd (70%) on behalf of joint venture partner Shell UK Ltd (30%). The Cambo Field consists of vertically stacked, Hildasay Member sandstone reservoir units that overlie the Colsay Member Volcanic sequence (Fielding et al. 2014).

The Hildasay reservoir sands were deposited in the early Eocene during the onset of rifting of the North Atlantic Ocean. The sands rest upon the volcanic Colsay sequence and are the paralic deposits brought into the area as a consequence of the hot and humid climatic conditions

with high rainfall prevalent at the time resulting in abundant river and delta systems. The Hildasay sediments form an anticline draped over a Precambrian basement high in the southern part of the field comprising granodiorite dated at 1.3 Ga.

The Hildasay Member forms part of the Upper Flett Formation, deposited on top of the volcanics of the Colsay Member and overlain by the Cambo Sands of the Balder Formation (Fig. 2). Based upon datings of the underlying Colsay Member basalts and the overlying Balder Formation volcaniclastics, it is likely that the Hildasay Member was deposited over a time period of 200–250,000 years. The reservoir units were deposited shortly after the Paleocene-Eocene Thermal Maxima (PETM) when global temperatures were 5–8 °C warmer than at present (McInerney and Wing, 2011) which may account for humid conditions resulting in higher rainfall during this period (Schmitz and Pujalte, 2007). The Hildasay reservoir sands were deposited in a paralic environment (fluvial-deltaic-estuarine) intercalated with field-wide claystones, siltstones and coals. The reservoir has been subdivided into several units from the H10/H20 basal unit to the H70 uppermost part of the Hildasay Member (Fig. 3). The reservoir is currently at a depth of ~2400 m TVDSS, in a water depth of ~1000 m. Fig. 4 shows the top field structure map and the location of the wells drilled to date. The oil present in the Cambo Field is moderately biodegraded with a gravity of 22–25 API and a viscosity of 3–12 cP at reservoir conditions. Organic geochemistry of the oils has proven an invaluable tool in determining reservoir connectivity and has shown that the main reservoir units are not in vertical communication but have geochemically distinct oils.

The main focus of this paper is the interval comprising the H50 and H40 units that form one of the major oil-bearing sequences in the field, but also contain the most carbonate-cemented intervals. The H50 and H40 sandstones are typically excellent reservoir quality sandstones with average core porosity of >30% and multi-darcy permeabilities. Sedimentological analysis of the core shows this interval consists of estuarine
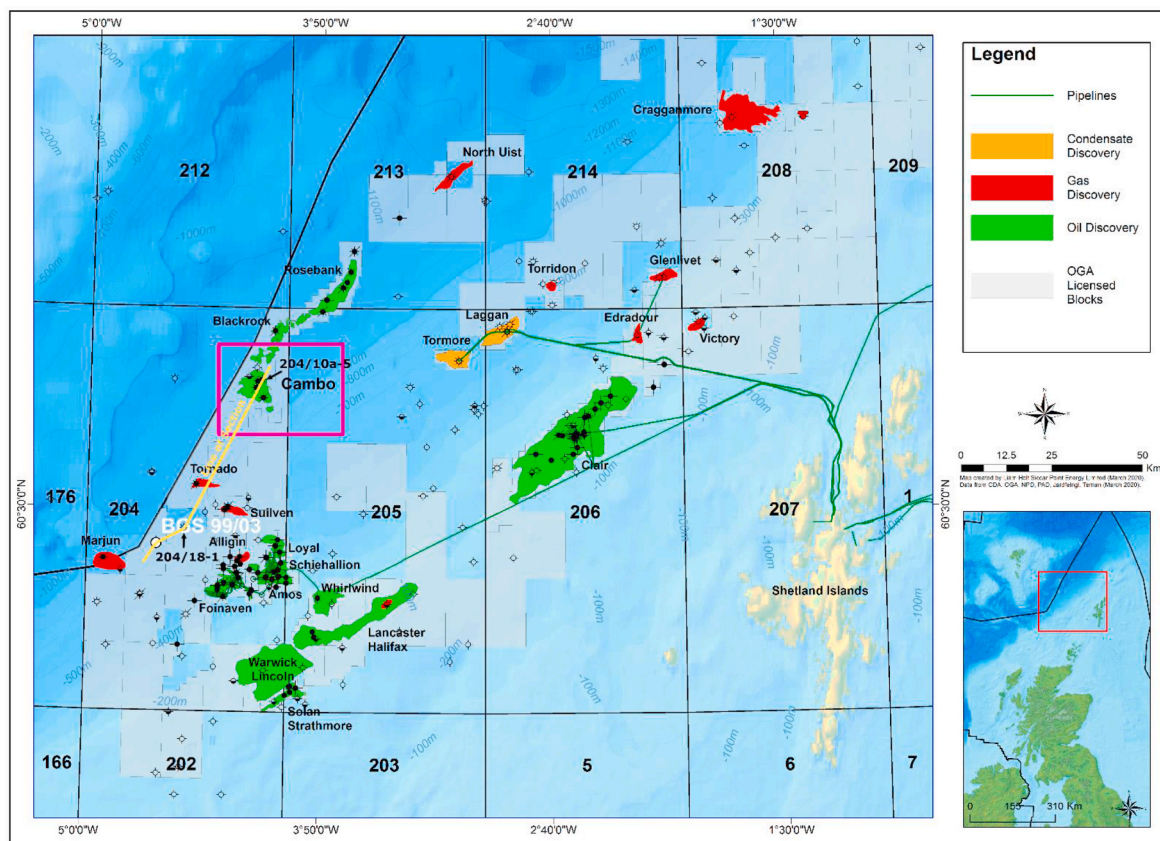

Fig. 1. Map showing location of the Cambo Field West of Shetlands (line of section shown in Fig. 12).

Fig. 2. Stratigraphic column of the strata present around the Cambo Field showing the subdivision of the Hildasay Member as utilised in this study. Stratigraphic ages from International Stratigraphic Chart v2019/05 (Cohen et al. 2013).

channel deposits with a high net-to-gross. Coals and claystones are locally developed at the top and base of the units, and act as barriers to vertical flow. The zone that contains the most carbonate-cemented sandstones occurs at the boundary between the H40 and H50 and can be seen in the log character and core across the northern part of the field (Fig. 5).

3. Samples and methods

This study is based upon core samples taken from the 204/10a-5 appraisal well drilled in 2018. Eight core plug samples were taken from the uncemented sandstone from the major reservoir units to confirm the mineralogy and texture of the sandstone, and five core plug samples were taken from the thickest carbonate-cemented interval encountered in the cored interval. Samples taken from the cemented interval were taken at regular intervals to establish if there was any systematic variation in the mineralogy or isotopic composition of the cemented interval. The core photograph and sample locations taken in the concretion are shown in Fig. 6.

The samples were analysed by a number of different methods including;

(1) Whole rock X-Ray Powder Diffraction (XRPD),
(2) Clay fraction (<2 μm) X-Ray Diffraction,
(3) Scanning Electron Microscopy SEM (both secondary electron analysis of fracture samples and back-scattered electron microscopy (BSEM) analysis of polished sections),
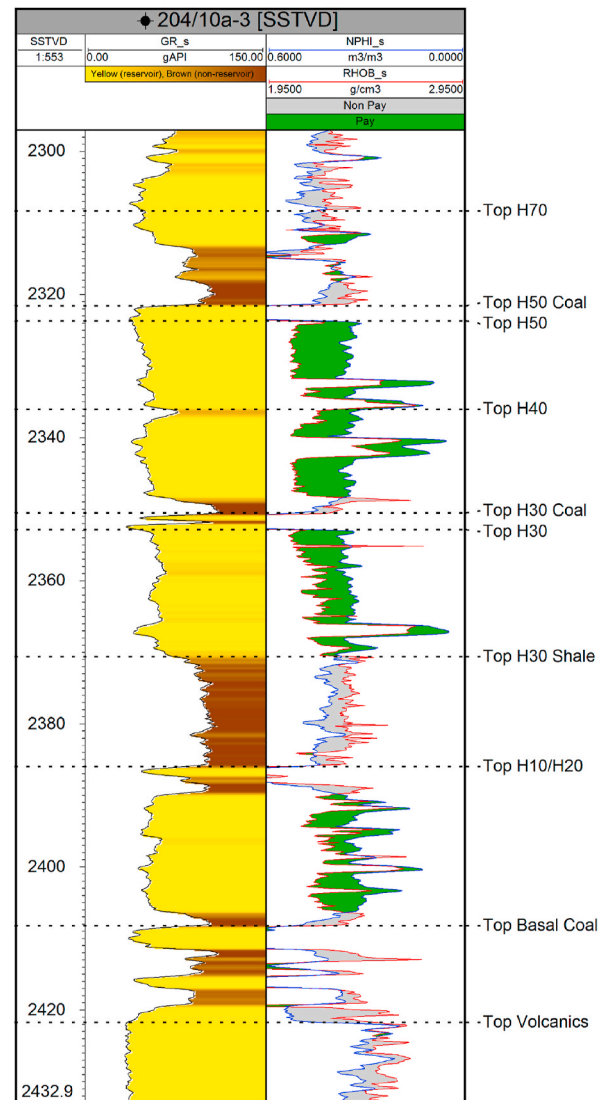

Fig. 3. Type log of the Hildasay Member in the Cambo Field showing reservoir sands separated by field wide extensive coals and shales. Main zone of interest for this study is the H40 and H50 intervals. Petrophysical logs displayed are gamma ray (GR), Neutron porosity (NPHI) and Density (RHOB). Reservoir sands are predominantly low gamma ray (yellow fill). (For interpretation of the references to colour in this figure legend, the reader is referred to the Web version of this article.)

(4) Energy Dispersive Spectroscopy (EDS) analysis of samples in the SEM was also utilised to determine the chemical composition of the different mineral phases,
(5) Thin section petrographic analysis,
(6) Petrographic cold cathodoluminescence of polished sections,
(7) Carbon, oxygen and clumped isotopic analysis.

Appendix A outlines the techniques used and the establishments where these analyses were undertaken. Appendix B reports the isotopic analysis techniques in detail. Tables 1–3 show the XRPD results, and Table 4 the isotopic analytical results.

4. Petrographic results

4.1. Uncemented sandstone

Samples were analysed from the uncemented sandstone to discern the detrital and authigenic mineralogy and whether this had any
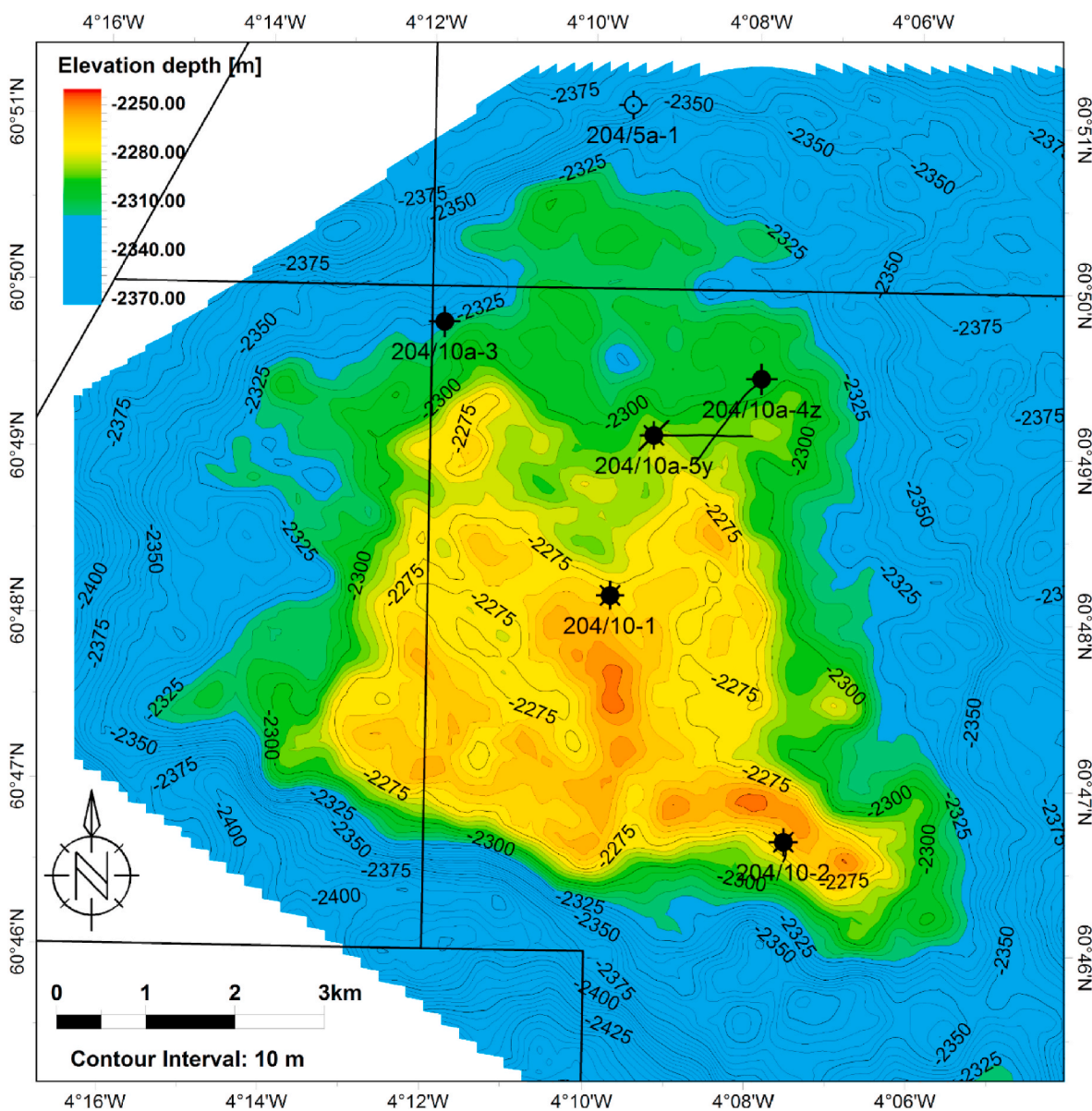
Fig. 4. Top H50 reservoir depth map of the Cambo Field showing location of wells. Study well is 204/10a-5 (pilot hole to 204/10a-5y).

influence on the presence or otherwise of any carbonate cementation. The quantitative mineralogy of the samples, both with respect to their detrital and authigenic composition, is shown in Tables 1 and 2.

4.1.1. Detrital mineralogy

All the reservoir sandstones examined are loosely packed and relatively unconsolidated, comprising sub-angular to sub-rounded grains. The Hildasay sandstones are second cycle deposits having been derived from Mesozoic rocks from the Scottish mainland. Biostratigraphic analysis has shown the sandstones to contain reworked terrestrial palynomorphs from Jurassic rocks (Jolley, 2012), with the likely source area being the Hebrides-Shetland Platform. The uncemented sandstones have been interpreted as the deposits of shoreface estuarine and fluvial channels. Texturally the sandstones are well to moderately well-sorted, and predominantly medium grained, although locally the grain size can range from coarse to fine. The sandstones analysed can be classified as subarkose to lithic subarkose using the classification of McBride (1963). Quartz is the dominant detrital mineral (average 70% with a range of 65–77%), with feldspar being the next most abundant (average 18%, range 13–24%). The dominant feldspar type is plagioclase (average

13%) with subordinate K-feldspar (average 5%). Thin section petrography shows ~10% of the detrital grains are lithic, comprising both igneous clasts (quartzo-feldspathic) and sedimentary (clay-rich clasts and chert).

4.1.2. Authigenic mineralogy

Pyrite – Authigenic pyrite is present in trace amounts (<1% by XRDP analysis) and most commonly occurs as framboids in primary pore space (Fig. 7a). The framboids are typically 20–40 μm in diameter, and are often associated with authigenic siderite and kaolinite (Fig. 7b).

Siderite – Siderite is present in trace amounts as clusters of lozenge-shaped euhedral crystals in primary pore spaces, often resting upon authigenic smectite that coats detrital grains (Fig. 7c). When analysed using BSEM the siderite crystals appear to be uniform with no obvious zonation (Fig. 7d). The average composition of the siderite from EDS analysis shows the crystals to have a high calcium and magnesium composition (Fe$_{64.7}$Ca$_{18.7}$ Mg$_{15.7}$ Mn$_{0.9}$), and as such can be termed sideroplesites (Deer et al., 1962).

Quartz – Quartz overgrowths occur as a minor diagenetic component (Fig. 7e), locally enclosing kaolinite crystals.
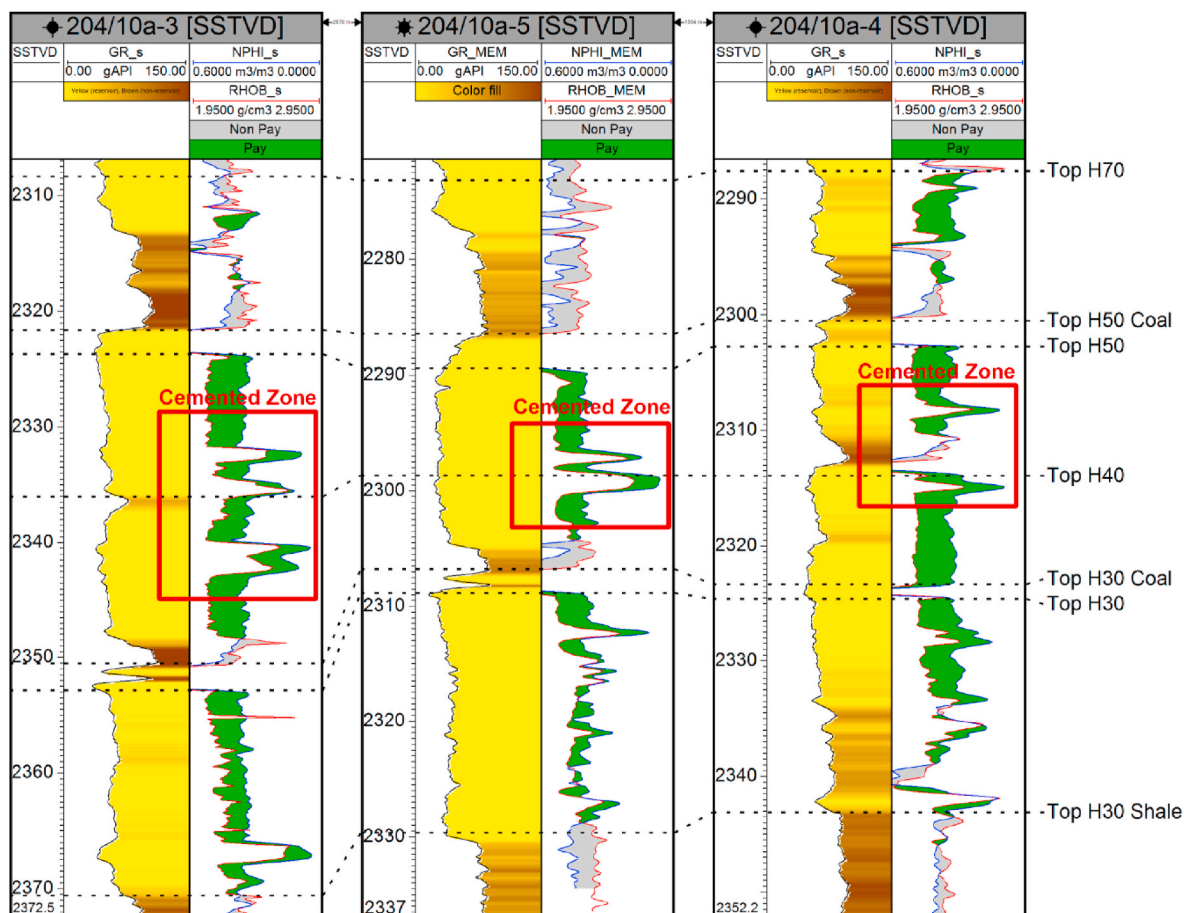
Fig. 5. Well correlation panel showing cemented zones located near the H40–H50 boundary in wells 204/10a-3, 2014/10a-5 and 204/10a-4 highlighted in red boxes. Cemented intervals are characterized by low porosity, high density and low gamma ray. Logs displayed are as outlined in Fig. 3. (For interpretation of the references to colour in this figure legend, the reader is referred to the Web version of this article.)

Smectite – Dioctahedral smectite occurs throughout the Hildasay reservoir sandstones in minor amounts (average 3%) as revealed by whole rock XRDP, clay fraction XRDP and SEM analysis. The smectite is pore-lining with a box-work like texture (Fig. 7f).

Kaolinite – Authigenic kaolinite is the dominant clay mineral present throughout the sandstone units (average 8%) where it occurs in primary pore space as verms and booklets (Fig. 7f). Locally the kaolinite rests upon the pore-lining smectite or is enclosed by quartz overgrowths (Fig. 7e).

4.2. Carbonate-cemented intervals

The carbonate-cemented interval that forms the basis of this study was sampled systematically, with a sample taken from the centre, two samples taken at the outer margins, and samples taken half-way between the margins and centre (the intermediate zone). The purpose of this approach was to determine whether there was any coherent variation in the mineralogy, composition of the cement and/or changes in isotopic composition across the cemented interval. The locations of the samples are shown in Fig. 6 and the whole rock XRDP analysis results shown in Table 3.

4.2.1. Core observations

The carbonate-cemented interval examined in this study is located close to the base of the H50 reservoir unit, with uncemented high porosity and high permeability sandstone both above and below. The cemented interval is 1.6 m thick in the core (Fig. 6), with a diffuse upper margin and a more distinct bedding parallel lower margin at the base.

The extensive carbonate cementation has obscured some of the primary sedimentary features, although it can be seen to comprise finer grained sands with local *Ophiomorpha* burrows. In addition, the interval contains scattered carbonaceous debris, locally concentrated in lags as evident in the centre of the interval. It is proposed that the interval was deposited under lower energy conditions compared to the main estuarine channel deposition of the uncemented sandstones, resulting in the finer grain size, burrowed nature of the sediments and the presence of the carbonaceous material.

4.2.2. Detrital mineralogy

The grain size and structure of the detrital component is very similar to that of the uncemented sandstones. Analysis of the slabbed core shows the cemented sandstone to be locally fine grained and mottled, with poorly defined burrows and scattered fine carbonaceous debris. The detrital mineralogy is dominated by quartz and feldspar. The detrital composition calculated from the XRDP data shows a quartz-feldspar composition of ~75% quartz to ~25% feldspar. Plagioclase is the dominant feldspar (~18%) with K-feldspar being subordinate (~6%) similar to the uncemented sandstones. A detrital component identifiable by the XRDP analysis that occurs in the centre of the cemented interval (sample C2) is carbonaceous woody organic matter (kerogen) that appears dark and relatively structureless in thin section. In this sample approximately 10–20% of the sample is composed of kerogen, although this may have been in part altered and replaced during diagenesis.

4.2.3. Authigenic mineralogy

Ferroan Calcite – The dominant cement in the carbonate-cemented
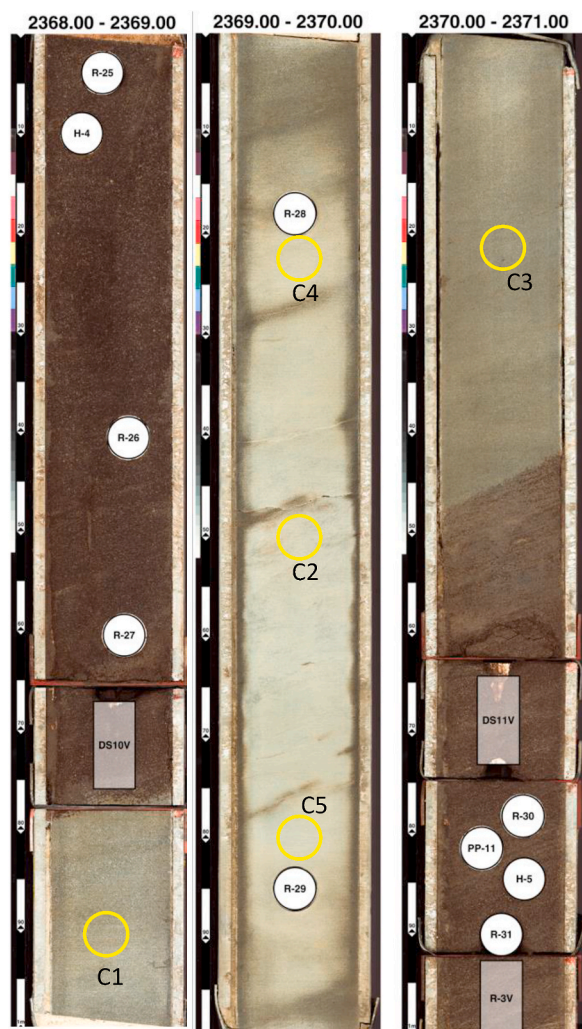
Fig. 6. Photograph of core from well 204/10a-5 showing light coloured cemented zone between brown, oil-stained uncemented sandstone. Sample locations for the concretion study are labelled C1–C5. Other plug samples have been taken for other core analyses. Core length = 1 m. Core depths shown at top of cored section in metres measured depth. (For interpretation of the references to colour in this figure legend, the reader is referred to the Web version of this article.)

intervals is ferran calcite that occurs as the major porosity occluding cement, occupying the primary porosity and is grain supporting (Fig. 8a, b). The XRDP analysis confirms the average calcite volume to be ~43% (weight %), although there is a marked spatial variation, with the centre of the cemented interval having the most (56%) and the margins of the cemented interval consistently having ~39%. The calcite is poikilotopic and appears uniform under BSEM analysis. The calcite also encloses the other authigenic phases including pyrite and kaolinite (Fig. 8b), and it

appears to locally replace siderite. The composition of the calcite from EDS analysis also reveals a spatial variation, with the centre sample being most ferroan (Ca $_{92.0}$ Fe $_{6.0}$ Mg $_{2.0}$ Mn $_{0.0}$), with less iron present in the outer margins (C1 sample = Ca $_{96.40}$ Fe $_{2.1}$ Mg $_{0.7}$ Mn $_{0.8}$, C2 sample = Ca $_{96.0}$ Fe $_{2.6}$ Mg $_{1.0}$ Mn $_{0.6}$). Chemical analysis of the calcite within each sample by EDS and as visualised utilising the BSEM supports the homogeneity of the cement, which is further confirmed by the Cathodoluminescence (CL) response. When analysed under CL all the calcite samples analysed have the same dull red luminescence with no obvious zonation (Fig. 8c, d).

Pyrite – As observed in the matrix sandstone, authigenic pyrite occurs as trace amounts in the calcite-cemented intervals as framboids typically encased by calcite (Fig. 8e). The highest concentration of pyrite from XRDP analysis is in the centre of the cemented interval (0.7%).

Siderite – After the ferroan calcite, siderite is the most dominant authigenic cement in the calcite-cemented interval. XRDP analysis reveals the central sample to contain ~13 wt% siderite, that under thin section appears as sphaerosiderite (Fig. 8f). The sphaerosiderite is associated with the kerogen and amorphous material when observed under thin section and BSEM analysis (Fig. 9a). Analysis by EDS of the sphaerosiderite shows it to be distinct from the euhedral siderite present in the uncemented sandstone, being higher in iron and calcium, but significantly lower in magnesium (Fe $_{71.3}$Ca$_{23.8}$ Mg$_{4.4}$ Mn$_{0.4}$). Although trace amounts of siderite were recorded in the XRD analysis of the other cemented samples, analysis of the sections utilising BSEM failed to reveal any samples suitable for EDS analysis.

Kaolinite – Authigenic kaolinite (average 2.5%) comprises verms and booklets enclosed by the ferroan calcite (Fig. 9b).

Smectite – Although dioctahedral smectite has been identified by XRDP analysis (trace to 7.6%) SEM analysis has not been able to reveal this authigenic phase. It should be noted that the smectite is most abundant in the centre of the cemented zone (7.6%) compared to the margins (2.9% to trace amounts).

5. Isotopic analysis

We have measured $\delta^{13}C$, $\delta^{18}O$ and Δ_{47} of the ferroan calcite. The carbon isotope composition represented by $\delta^{13}C$ is used to help determine the dominant source of carbon (inorganic or organic) and the dominant processes likely to have been active at the time of precipitation (e.g. aerobic and anaeorobic oxidation pathways for organic matter,

Table 2
Clay fraction (<2 μm) XRDP Results – Matrix Sandstone samples (weight %).

Sample	Depth	Unit	Chlorite	Kaolinite	Illite	Smectite
H-1	2361.2	H50	Trace	10	Trace	90
H-3	2366.7	H50	1	42	1	56
H-4	2368.1	H50	Trace	51	1	48
H-5	2370.8	H40	Trace	64	1	35
H-6	2372.1	H40	Trace	68	2	30
H-7	2379.3	H30	Trace	85	1	14
H-8	2380.5	H30	Trace	85	2	13
H-9	2381.5	H30	Trace	78	4	18

Table 1
Whole rock XRDP Results – Matrix Sandstone samples (weight %).

Sample	Depth	Unit	Quartz	Plagioclase	K-feldspar	Calcite	Siderite	Pyrite	Smectite	Kaolinite
H-1	2361.2	H50	75.9	9.5	3.3	0.2	1.0	0.1	4.9	4.5
H-3	2366.7	H50	69.4	11.7	5.4	0.0	0.0	0.5	5.3	7.4
H-4	2368.1	H50	76.6	9.8	4.5	0.2	0.0	0.1	1.7	6.8
H-5	2370.8	H40	73.1	11	5.7	0.0	0.0	0.1	2.7	7.1
H-6	2372.1	H40	69.4	12.9	5.7	0.0	0.0	0.2	2.4	9.0
H-7	2379.3	H30	68.2	13.4	5.4	0.0	0.0	0.8	2.7	9.3
H-8	2380.5	H30	65.8	15.3	5.2	0.4	0.0	0.3	2.5	10.1
H-9	2381.5	H30	62.9	17.6	6.3	0.7	0.0	0.4	2.2	9.6

Table 3
Whole rock XRDP Results – Carbonate Concretion samples (weight %).

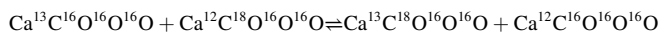| Sample	Depth	Quartz	Plagioclase	K-feldspar	Calcite	Siderite	Pyrite	Smectite	Kaolinite
C-1	2368.9	43.4	9.8	3.6	39.8	0.0	0.0	trace	3.4
C-4	2369.2	41.2	9.9	3.2	39.5	1.0	0.0	2.9	2.0
C-2	2369.5	12.5	5.9	2.1	56	12.8	0.7	7.6	1.8
C-5	2369.8	42.3	11.1	2.7	38.9	1.1	0.0	1.4	2.1
C-3	2370.2	44.3	8.2	2.8	39.6	0.5	0.1	1.5	3.0

Table 4
Bulk and clumped isotope data summary. n is the number of sample replicates analysed. Numbers in brackets are the $\pm$ one standard error measurement uncertainty for δ^{13}C, δ^{18}O, Δ_{47} and Δ_{48} based on replicate analysis of n samples. The error in T and the Fluid-δ^{18}O value is based on propagation of the measurement uncertainties. Δ_{47} values are given with respect to the CDES scale and calibrated using carbonate standards ETH1, ETH3 and the UEA internal laboratory standard ueacmst. Δ_{48} values are reported with respect to the local working reference gas frame. The reference gas is prepared from BDH marble chips by reaction with phosphoric acid followed by equilibration with water, both at room temperature.

Sample	Depth (m)	N	$\delta^{13}C_{VPDB}$	$\delta^{18}O_{VPDB}$	Δ_{47}	Δ_{48}	$T\,^\circ C$	Fluid-$\delta^{18}O_{VSMOW}$
C-1	2368.9	4	−15.52 (0.02)	−12.20 (0.02)	0.592 (0.008)	−0.258 (0.050)	48.3 (3.6)	−5.5 (0.6)
C-4	2369.2	4	−3.68 (0.02)	−10.97 (0.02)	0.611 (0.024)	−0.232 (0.021)	40.5 (9.6)	−5.7 (1.8)
C-2	2369.5	4	+7.53 (0.05)	−11.05 (0.03)	0.600 (0.022)	−0.205 (0.034)	45.0 (9.1)	−5.0 (1.6)
C-5	2369.8	5	+0.72 (0.02)	−11.48 (0.06)	0.592 (0.014)	−0.289 (0.03)	48.6 (6.2)	−4.8 (1.1)
C-3	2370.2	4	−15.87 (0.28)	−12.01 (0.10)	0.585 (0.013)	−0.216 (0.054)	51.3 (5.9)	−4.8 (1.0)

bacterial methanogenesis and fermentation) with the carbon isotope composition being very distinct for the different biologic pathways (e.g. see Irwin et al., 1977; Coleman and Raiswell, 1993).

The δ^{18}O of the cement calcite is determined by the isotopic composition of the precipitating fluid and the temperature at which precipitation occurred. An independent measurement of precipitation temperature allows the oxygen isotopic composition of the parent fluid to be estimated using the δ^{18}O of the calcite and empirically determined fractionation factors for ^{18}O partitioning between calcite and water.

To estimate the growth temperature, we have measured the clumped Δ_{47} of CO_2 produced by reaction of the cements with ortho-phosphoric acid. This parameter is directly related via an acid fractionation factor with Δ_{63}, a measure of the degree of ordering of the ^{13}C and ^{18}O amongst the available sites in the carbonate lattice. At sufficiently high temperatures ^{13}C and ^{18}O are randomly distributed amongst all the possible sites within the lattice. As temperatures cool the lower bond energy between ^{13}C and ^{18}O results in a non-random distribution, or clumping of the isotopes (Schauble et al., 2006; Eiler, 2007). This clumping is described by the order-disorder reaction:

$$Ca^{13}C^{16}O^{16}O^{16}O + Ca^{12}C^{18}O^{16}O^{16}O \rightleftharpoons Ca^{13}C^{18}O^{16}O^{16}O + Ca^{12}C^{16}O^{16}O^{16}O$$

The reduced enthalpy due to the ^{13}C – ^{18}O bond is sufficient to overcome the loss of entropy associated with the more ordered state represented by the right-hand side of the reaction. Equilibrium favours clumping with the degree of clumping increasing as temperature decreases. The important aspect of the order-disorder reaction is that it represents a homogenous isotope exchange reaction between sites in the carbonate lattice and can be used as the basis of a geothermometer. Measurement of the degree of ordering can directly be translated to a temperature. In contrast the carbonate oxygen isotope geothermometer relies on determining the fractionation of ^{18}O between a mineral and fluid phase which, in practice, requires knowledge of both the mineral and fluid oxygen isotope compositions.

Analytically, the degree of clumping is represented by Δ_{47} of the CO_2 released by reaction of the sample with ortho-phosphoric acid. It is defined as:

$$\Delta_{47} = \left(\frac{R^{47}}{(R^{47})^*} - 1\right) \times 1000$$

R^{47} is the measured 47/44 ratio of the analyte CO_2 and $(R^{47})^*$ is the ratio one would expect for a random, or stochastic distribution. The stochastic distribution is calculated using the measured R^{13} ($^{13}C/^{12}C$)

and R^{18}O ($^{18}O/^{16}O$) ratios of the sample. Δ_{47} is inversely proportional to T^2 with a total range in Δ_{47} of <0.5‰ for temperatures between $0\,^\circ$C and high temperatures, >$600\,^\circ$C. Temperature sensitivity is close to -0.003‰ per $^\circ$C at ambient surface temperatures ($20\,^\circ$C), decreasing to -0.0015‰ per $^\circ$C at $100\,^\circ$C.

Whilst still a novel technique there have been a significant number of studies using the clumped isotope geothermometer. Many of these have been targeted at determining Earth surface temperatures as part of paleoclimate studies with a smaller subset of studies with diagenetic, mineralization and tectonic processes. These include Bristow et al. (2011), Loyd et al. (2014), Huntington and Lechler (2015), Luetkemeyer et al. (2016), Dennis et al. (2019) and Veillard et al. (2019).

The bulk and clumped isotope data are summarized in Table 4 and in plots of δ^{13}C, δ^{18}O, T and $\delta^{18}O_{fluid}$ versus depth (Fig. 10(a)), δ^{13}C versus δ^{18}O (Fig. 10(b)), T versus δ^{13}C (Fig. 10(c)) and T versus δ^{18}O (Fig. 10 (d)).

The δ^{13}C of the cements covers a wide range from +7.5‰ to −15.9‰ with a marked systematic variation within the cemented unit (Fig. 10(a), (b)). The centre of the unit (C2) is enriched in ^{13}C (+7.54‰) whilst the upper and lower margins are significantly depleted with a δ^{13}C of −15.9‰ (C1) to −15.5‰ (C3). Between the margins and centre the cement has an intermediate δ^{13}C of +0.7‰ (C4) and −3.7‰ (C5). The overall pattern is symmetric about the centre suggesting that cementation progressed outwards from a core and was accompanied by an increasing depletion in ^{13}C from an initial positive δ^{13}C to negative values (Fig. 10(a)).

In contrast the oxygen isotope composition of the cement has a narrow range in δ^{18}O of 1‰ from −11‰ in the core of the unit (C2 and C4) to −12‰ (C3) and −12.2‰ (C1) at the bottom and top margins respectively (Fig. 10(a), (b)). Sample C5 has an intermediate δ^{18}O of −11.5‰. The narrow range in δ^{18}O and the observation that the distribution of δ^{18}O is not as markedly defined as δ^{13}C suggests that precipitation of the cement occurred over a limited range of temperatures and from pore fluids with a restricted range of oxygen isotope composition.

This is supported by the clumped isotope Δ_{47} data which ranges from 0.585‰ to 0.611‰ (Table 4). The 1σ standard error uncertainty for these samples is between ±0.008‰ and ±0.024‰. Thus, the Δ_{47} of the samples can not statistically be distinguished. The mean Δ_{47} of all the samples is 0.596‰ (±0.007‰, n = 21). However, whilst we note the similarity of the data there is a systematic pattern with the more positive Δ_{47} associated with samples in the interior of the cemented unit and the
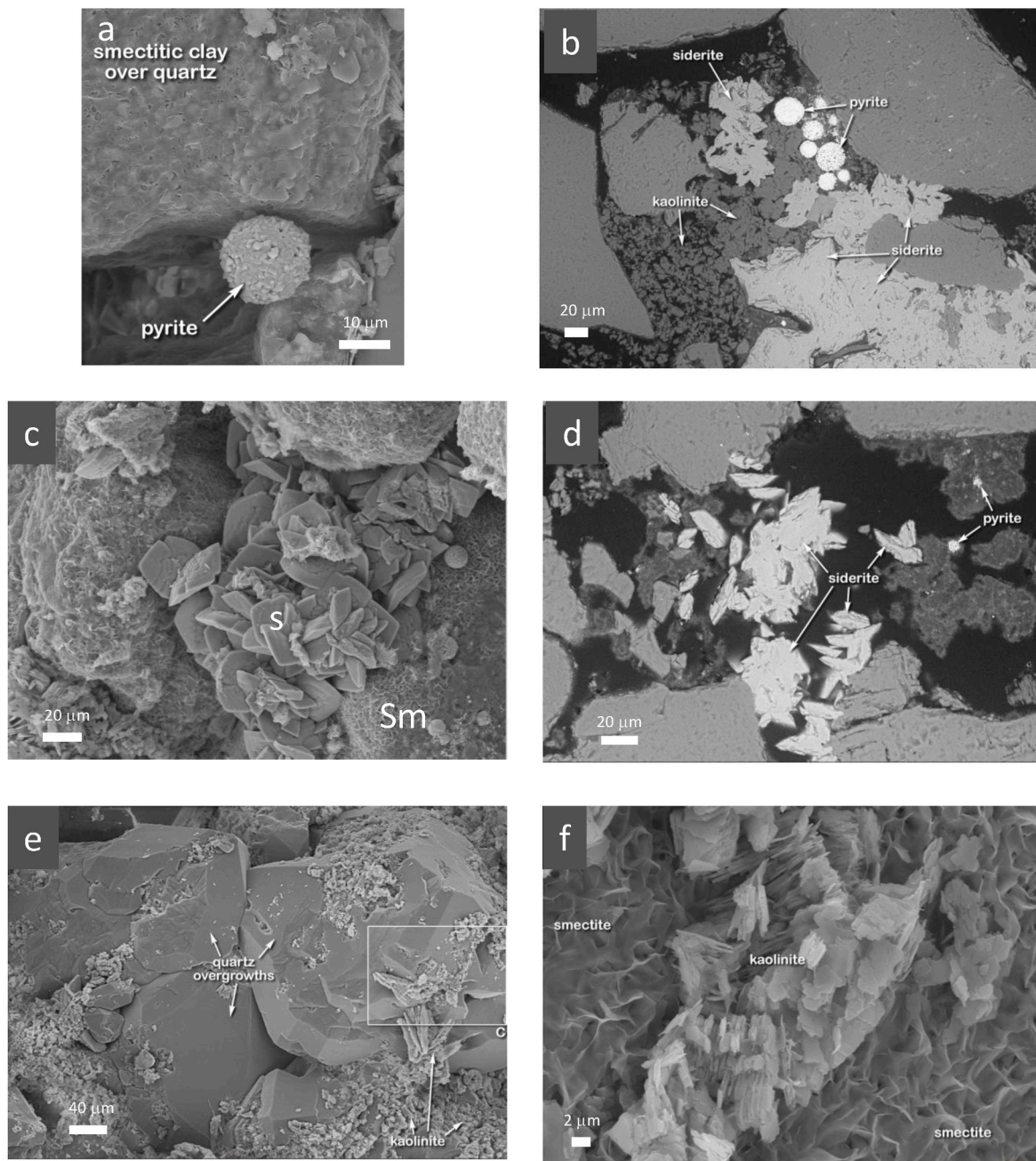
Fig. 7. a. SEM image of pyrite framboid in primary pore space, resting on smectitic clay in matrix sandstone. Scale bar 10 μm. Sample H6, 2372.14 m, 204/10a-5. (7b) BSEM image of polished section showing framboidal pyrite enclosed by authigenic kaolinite and siderite. Scale bar 20 μm. Sample H1, 2361.19 m, 204/10a-5. (7c) SEM image of lozenge shaped siderite crystals (s) resting on grains coated with smectite (Sm). Scale bar 20 μm. Sample H1, 2361.19 m, 204/10a-5. (7d) BSEM image of polished section showing uniform composition of siderite in primary pore space. Scale bar 20 μm. Sample H1, 2361.19 m, 204/10a-5. (7e) SEM image of quartz overgrowths partially enclosing authigenic kaolinite. Scale bar 40 μm. Sample H7, 2379.32 m, 204/10a-5. (7f) SEM image of kaolinite platelets resting on grain-coating smectite. Scale bar 2 μm. Sample H1, 2361.19 m, 204/10a-5.

lower values associated with the two samples located on the margins of the unit (C1 and C3).

This pattern is clearly seen when converting Δ_{47} to temperature, T (Δ_{47}) (Fig. 10(a), (c) and (d)). The interior of the cemented unit formed at a temperature between 40 °C and 45 °C (C2 and C4), whilst the margin cements (C1 and C3) precipitated at a temperature of approximately 50 °C. C5, intermediate between C2 in the centre of the cemented layer and the margin, precipitated at a temperature of 48 °C. The distribution of temperature inversely covaries with $\delta^{18}O$ of the ferroan calcite cement (Fig. 10(a)).

Fluid oxygen isotope compositions, calculated using T(Δ_{47}) and $\delta^{18}O$

of the calcite cement range between $\delta^{18}O$ of $-4.8‰_{VSMOW}$ and $-5.7‰_{VSMOW}$ (Fig. 10(a) and (d)), with a mean value of $-5.2‰$ ($\pm0.42‰$, 1σ, n = 5). In Fig. 10(d) we have plotted T(Δ_{47}) *versus* $\delta^{18}O$ of the ferroan calcite. The contours on the plot are isopleths of fluid $\delta^{18}O$. Here we see that the cement grew under a near constant fluid oxygen isotope composition, evolving from a $\delta^{18}O$ of $-11‰$ in the centre to $-12‰$ at the margin as temperature increased from 40 °C to 50 °C.

6. Discussion

The reservoir of the Cambo Field is dominated by poorly cemented
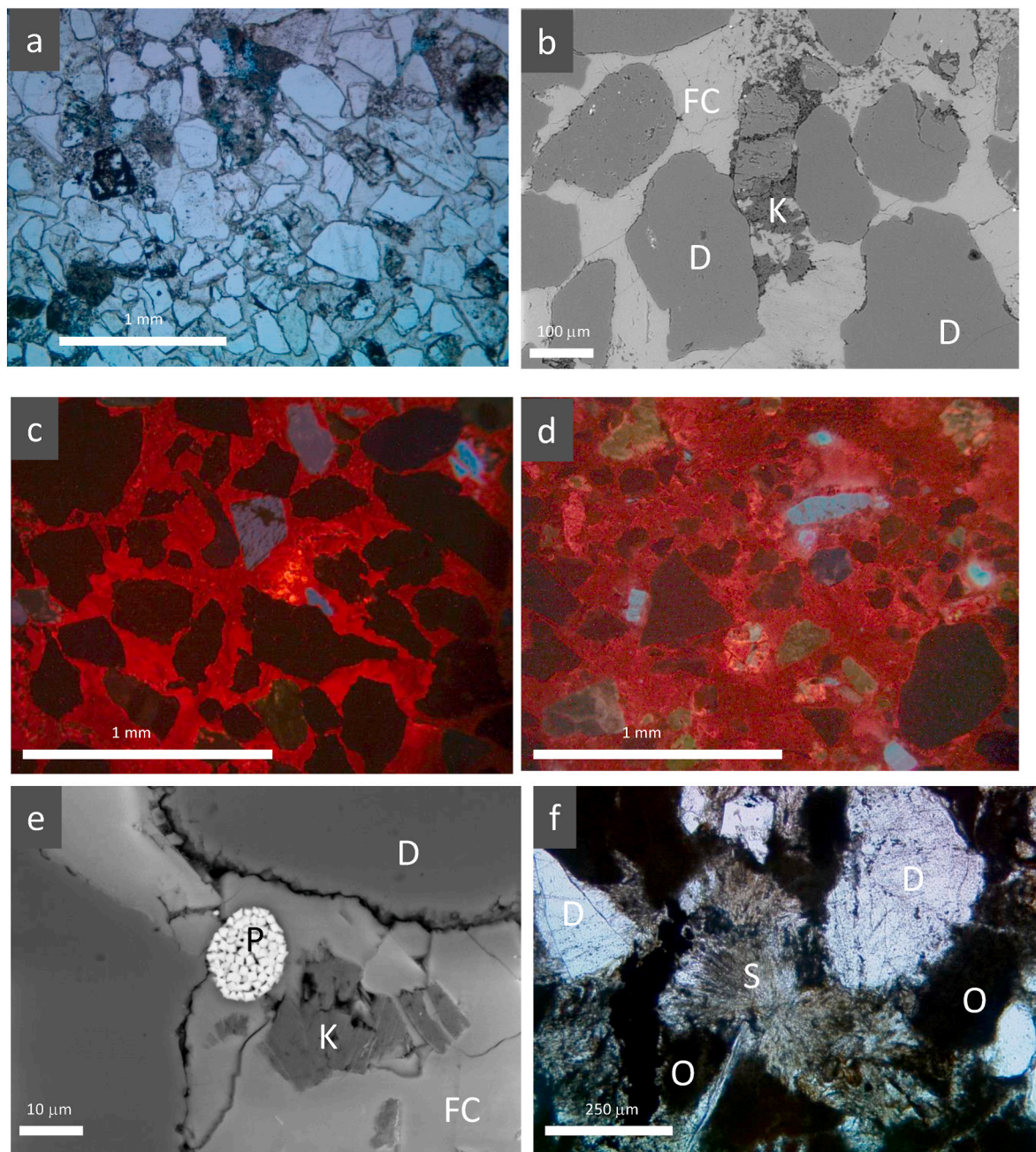
Fig. 8. a. Photomicrograph of thin section (plane polarised light) showing detrital grains with all porosity occluded by ferroan calcite. Scale bar 1 mm. Sample C1, 2368.9 m, 204/10a-5. (8b) BSEM of polished section showing Ferroan Calcite (FC) occupying all the primary porosity and enclosing authigenic kaolinite (K). Scale bar 100 μm. Sample C1, 2368.9 m, 204/10a-5. (8c) Cathodoluminescent photomicrograph of extensive ferroan calcite from upper margin of cemented unit showing homogeneous dull red luminescence. Scale bar 1 mm. Sample C1, 2368.9 m, 204/10a-5. (8d) Cathodoluminescent photomicrograph of extensive ferroan calcite from centre of cemented unit showing homogeneous dull red luminescence. Scale bar 1 mm. Sample C2, 2369.5 m, 204/10a-5. (8e) BSEM image of polished section showing framboidal pyrite (P) enclosed by ferroan calcite (FC). Calcite also encloses authigenic kaolinite (K). Detrital grains (D). Scale bar 10 μm. Sample C1, 2368.9 m, 204/10a-5. (8f) Photomicrograph of thin section (plane polarised light) showing sphaerosiderite (S) and organic matter (O). Detrital grains (D). Scale bar 250 μm. Sample C2, 2369.5 m, 204/10a-5. (For interpretation of the references to colour in this figure legend, the reader is referred to the Web version of this article.)

sandstones with a low degree of compaction and cementation. Consequently, the reservoir quality is excellent with high porosity (30%) and permeability (multi-darcy) and is only poor quality where extensively cemented by ferroan calcite. Analysis of the cemented and non-cemented sandstones shows a similar sequence of authigenic minerals that formed during early diagenesis, including pyrite, siderite, kaolinite and smectite. Where uncemented, the smectite can be observed as a grain-rimming cement that was an early diagenetic phase. The subsequent authigenic minerals pyrite, siderite and kaolinite can often be observed to rest on the smectite, and hence post-date it.

The origin of the pyrite framboids is interpreted to have been during early diagenesis, with the sulphate required being present in the seawater introduced during marine incursions. Sulphate reducing bacteria would have created the reducing conditions for the pyrite to have formed (Picard et al., 2018). As the sulphate in the porewaters was consumed it is likely that methanogenesis will have commenced and any iron present incorporated into siderite. The sphaerosiderite, observed in the cemented sandstone but not in the uncemented sandstone, is morphologically distinct and is associated with the kerogen and amorphous matter in the centre of the cemented interval. Spherulitic siderite
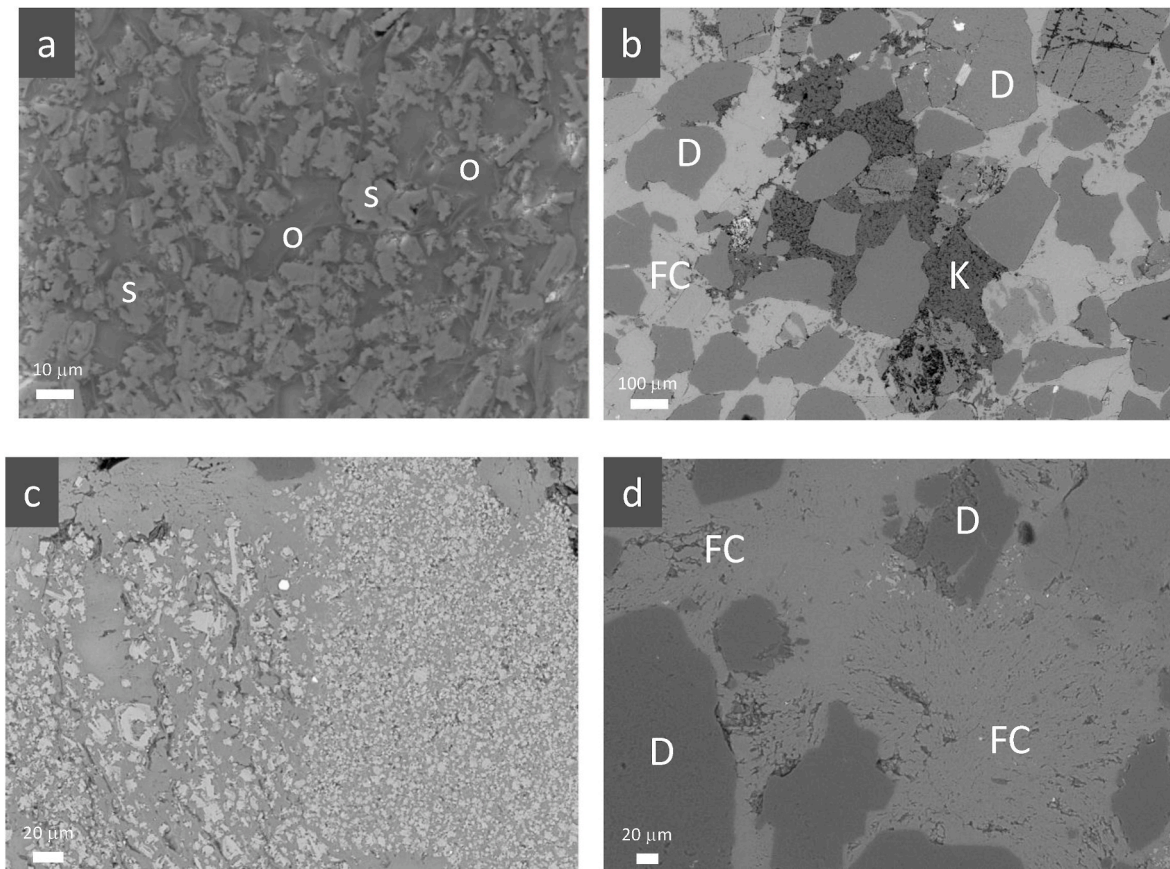
Fig. 9. a. SEM image of polished section showing siderite (s) and organic matter (o) intricately admixed. Scale bar 10 μm. Sample C2, 2369.5 m, 204/10a-5. (9b) BSEM image of polished section showing ferroan calcite (FC) enclosing authigenic kaolinite (K). Detrital grains (D). Scale bar 100 μm. Sample C1, 2368.9 m, 204/10a-5. (9c) BSEM image of polished section showing admixed Ferroan calcite (grey) and siderite (light grey). Scale bar 20 μm. Sample C2, 2369.5 m, 204/10a-5. (9d) BSEM image of polished section showing sphaerosiderite texture replaced by ferroan calcite (FC). Detrital grains (D). Scale bar 20 μm. Sample C2, 2369.5 m, 204/10a-5.

forms predominantly in wetland soils and sediments (Ludvigson et al., 1998) and has been reported in a number of present-day intertidal marsh and sandflat sediments (Pye et al., 1990; Moore et al., 1992). Consequently, it would be expected to have precipitated in the marshy and waterlogged sequences of the Hildasay units. Ancient sphaerosiderites are found in paleosol horizons within coal-bearing stratigraphic intervals interpreted as having formed in water-saturated environments, similar to the Hildasay units. Analysis by EDS has shown that this phase of siderite has significantly more iron and less magnesium compared to the lozenge shaped siderite crystals observed in the uncemented sandstone, suggesting a change in the porewaters between precipitation of the two forms of siderite. The increase in magnesium in the "lozenge" siderite could have resulted from an increase in marine water porewaters, compared to a more fluvial origin for the waters present during the precipitation of the sphaerosiderite.

The kaolinite observed in the Hildasay sandstones, both in the carbonate-cemented and uncemented sandstones appears as booklets, typically of fine plates. The booklets locally appear in a vermiform texture, and probably have resulted from the alteration of detrital feldspars. The fine vermiform nature of the kaolinite would suggest a low temperature origin; thicker, blockier kaolinites are more often associated with a high temperature of formation (Lanson et al., 2002).

Quartz is a minor authigenic component of the sandstones and may be a by-product of the alteration of the feldspars to authigenic clays (smectite and kaolinite). As the quartz overgrowths locally enclose kaolinite it can be assumed that it's precipitation in part post-dated the formation of the kaolinite.

The ferroan calcite formation appears, based upon the textural relationships, to be a later diagenetic event as it is observed to enclose the other authigenic minerals (kaolinite, pyrite). The calcite also, from cathodoluminescence (CL) observations, appears to have formed as a single phase, with no distinction or zonation observed between the calcite in the core of the cemented interval, and that observed at the margins. The calcite in the centre of the cemented interval has a complex relationship with the earlier formed siderite. When viewed under standard thin section petrography the centre of the cemented interval appears to comprise sphaerosiderite crystals, with amorphous and locally opaque organic matter (kerogen) and mudstone (Fig. 8f). Polished sections observed utilising SEM show the intimate relationship between the siderite and organic matter (Fig. 9a) with microcrystals of siderite intermixed with the thin lath-like fabric of kerogen. Under CL the centre of the concretion is dominated by red luminescent ferroan calcite, similar to that seen at the margins (Fig. 8c, d). Analysis by BSEM of the centre of the cemented interval also reveals that the sphaerosiderite fabric has been extensively replaced by ferroan calcite (Fig. 9c). It is possible that the intermixing of the siderite and ferroan calcite occurred during or soon after deposition, as both Moore et al. (1992) and Pye et al. (1990) report minor amounts of other carbonates (calcite, ankerite) precipitating with the siderite in the intertidal marsh sequences that they studied. As the siderite and ferroan calcite are intricately admixed, this may account for the siderite appearing to be "siderite" under standard petrographic analysis, but appearing luminescent under CL. Given the high iron content of siderite it is unlikely to luminesce under CL (Budd et al., 2000). Locally within the central part of the cemented interval the ferroan calcite appears to have completely replaced the siderite, leaving only an outline of the original sphaerosiderite (Fig. 9d).
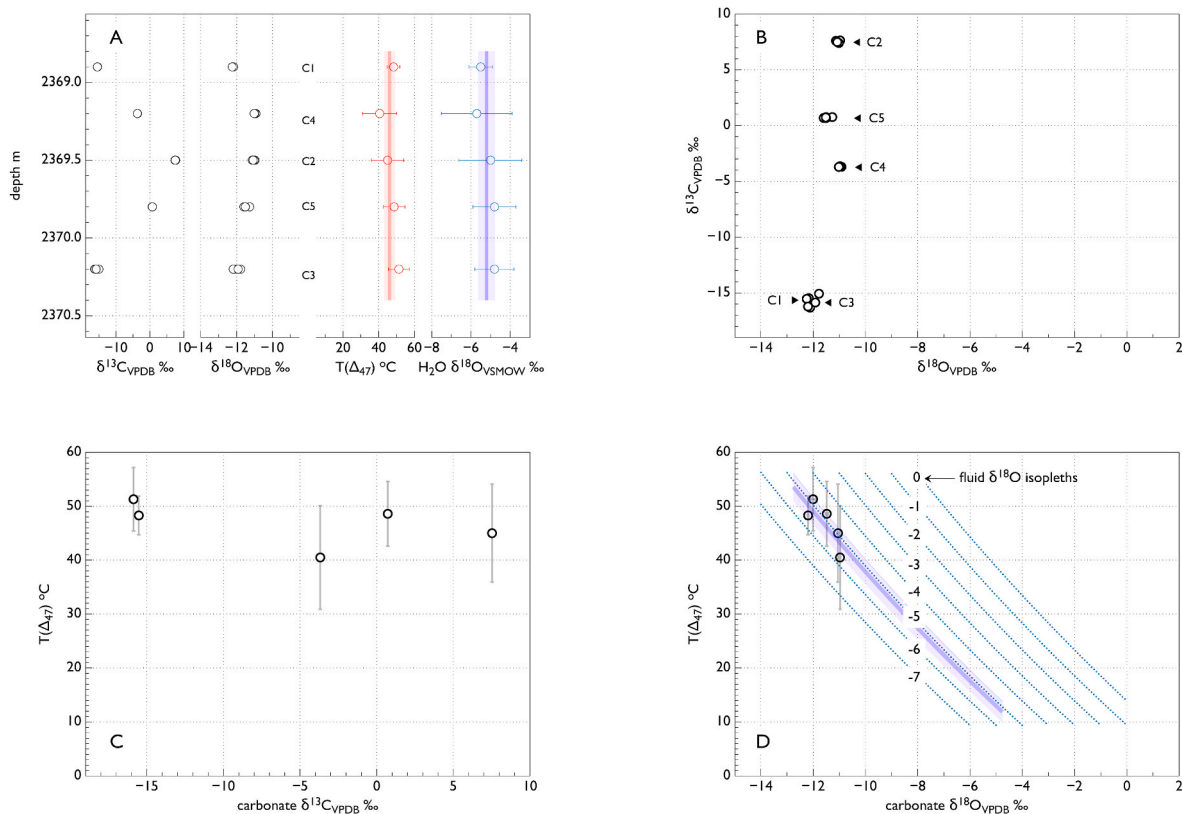
Fig. 10. (a) δ^{13}C, δ^{18}O, T(Δ_{47}) and δ^{18}O$_{\text{fluid}}$ v. Depth. The solid vertical lines and shaded regions represent the mean temperature (red) and fluid δ^{18}O (blue) and their associated uncertainty ($\pm$1s.e.). The samples and their associated depths are identified. (b) δ^{13}C v. δ^{18}O, (c) T(Δ_{47}) v. δ^{13}C, (d) T(Δ_{47}) v. δ^{18}O$_{\text{carbonate}}$. The isopleths are lines of constant δ^{18}O$_{\text{fluid}}$ in ‰ wrt VSMOW. The cements lie along a trajectory of near constant fluid isotope composition that is characteristic of high fluid:rock ratios and with a value of -5.2 ± 0.42‰ (blue solid line and shaded region), consistent with a significant meteoric component to the pore fluid. (For interpretation of the references to colour in this figure legend, the reader is referred to the Web version of this article.)

Analysis by EDS also shows a variation in the chemical composition of the ferroan calcite, with the calcite in the centre of the cemented interval containing more iron and magnesium than the calcite located at the margins. Notwithstanding this variation in composition, the calcite exhibits similar luminescence at the centre and margins of the cemented interval.

The carbon isotopic analysis of the ferroan calcite would suggest that the calcite that precipitated in the centre of the concretion did so under significantly different porewater conditions to that prevalent during the later phases of calcite cementation. The carbon isotopic composition of the calcite analysed from the centre has a high δ^{13} carbon composition (δ^{13} C$_{\text{VPDB}}$ = 7.53‰) typical of anaerobic methanogenesis or anaerobic fermentation (Coleman and Raiswell, 1981). The intermediate zone has a lower δ^{13} carbon isotopic composition (δ^{13} C$_{\text{VPDB}}$ = 0.72 to −3.68‰), and the calcite at the margins of the cemented interval has an even lower δ^{13} carbon isotopic composition (δ^{13} C$_{\text{VPDB}}$ = −15.52 to −15.87‰) more typical of a strong aerobic oxidation signal (Irwin et al., 1977). The oxygen isotopic signature of the ferroan calcite throughout the unit is very similar (δ^{18} O$_{\text{VPDB}}$ = −10.97 to −12.20‰) and suggests that the active fluids during diagenesis had a significant meteoric component. This is supported by the clumped isotope analysis which shows limited variation within the cemented unit with a range of Δ_{47} values from 0.585 to 0.611. These results would indicate that the ferroan calcite precipitated over a relatively narrow temperature range (40–50 °C) from porewaters that had a markedly ^{18}O depleted character typical of meteoric waters (δ^{18} O$_{\text{VSMOW}}$ -4.8 to −5.7‰).

Key to understanding the timing and origin of the carbonate-cemented sandstones is an understanding of the burial and thermal history of the reservoir sands. The burial history of the Hildasay reservoir is relatively simple and is shown in Fig. 11. After deposition during

the early Eocene (~55 Mya) the interval was submerged during the Balder Formation transgression and continued to be buried by marine sediments. After an initial period of moderate burial rate, the burial rate slowed during the deposition of the Stronsay Group and recent sediments, combined with rising sea level that has left the Hildasay at its maximum burial depth (~2400 m TVDSS) and maximum temperature (~60 °C).

6.1. Carbonate cementation model

The central question to be addressed by this study was two-fold: (1) How did the carbonate cemented intervals in the Hildasay units form? And (2) are they laterally extensive such that they will impact hydrocarbon production?

Based upon the petrographic data it can be seen that the calcite precipitated as one of the last authigenic phases in the reservoir sandstones as it encloses the kaolinite, pyrite and siderite. The homogeneity in the CL response of the calcite and the consistency in the temperature of formation based upon the clumped isotope analysis also suggests that the calcite formed as a single event, although the geochemical and stable isotopic composition of the calcite suggests that the centre of the cemented interval formed under significantly different porewater conditions compared to the margins of the cemented interval. The possibility that the ferroan calcite is extensively recrystallised, and hence has a single CL response is unlikely given that recrystallisation typically requires a temperature of >100 °C (O'Neil, 1987), a temperature not experienced by the sediments during their burial history (maximum temperature ~60 °C), and significantly above that determined from the clumped isotope analysis.

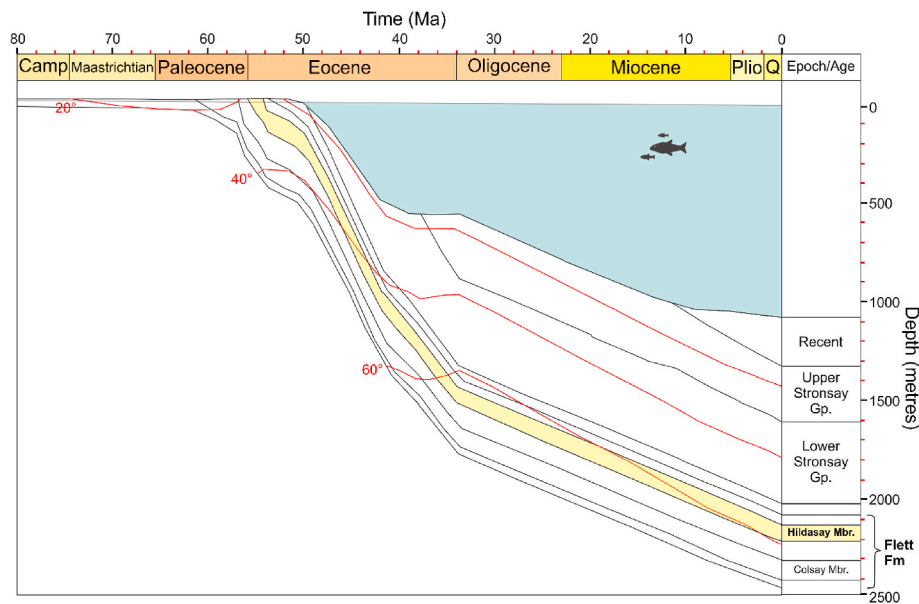Collating all the data and observations of the carbonate-cemented

Fig. 11. Burial curve showing isotherms for the Cambo Field. Based upon 204/10-1 well data.

sandstone interval studied, the following diagenetic model is proposed;

(1) Early diagenesis was focussed in the centre of the cemented interval where a thin lag of woody and finer grained material was cemented by siderite that formed in porewaters depleted in oxygen and sulphide and enriched in ferrous iron. The spherulitic form of the siderite reflects the marshy and water-logged conditions conducive to this crystal morphology. Pye et al. (1990) noted that a quarter of the siderite cementation that they observed in a modern-day marsh formed around fragments of wood. Pye et al. (1990) postulated that the presence of the wood may have played a significant role in the distribution and rate of bacterial activity including methanogenesis and fermentation. Intertidal sandflats, deltaic sediments and marshes typically contain sufficient ferrous iron to support siderite formation (Trefrey and Presley, 1982).

(2) Calcite precipitation commenced under similar conditions, with a high iron content and a high δ^{13} carbon isotopic composition, reflecting the anaerobic methanogenesis or fermentation processes active at the time. The shift from siderite formation to ferroan calcite may reflect a change in porewater chemistry and bacterial activity. Similar paragenetic sequences have been reported in modern marsh environments (Moore et al. 1992).

(3) It is likely that the early ferroan calcite acted as a nucleation site for the later calcite cementation that formed the cemented interval observed in the core. As the calcite continued to precipitate the porewaters became dominated by meteoric water with a distinctive isotopic signature that was progressively depleted in δ^{13} carbon and more aerobic. This mechanism of later calcite cementation, post-dating the sphaerosiderite, is supported by Wilkinson (1992) who suggested that where early diagenetic carbonates are present within a sandbody they will act as substrates for the nucleation of later carbonates by reducing the activation energy required to precipitate the later carbonate phase.

(4) If this model is correct, then the carbonate cemented horizons should be restricted to the intervals that contain woody material, i.e. fine-grained lag deposits in the estuarine channel sands. As such it would be expected, given the overall high energy of the estuarine channel deposits, that these intervals will be laterally limited in extent, and consequently the carbonate cementation will likewise not extend over large areas.

Although the model proposed above accounts for the petrographic observations, there remain two questions that need to be addressed, (1) What was the source of the meteoric aerobic pore-fluids that were dominant in the precipitation of the calcite? And (2) Is the temperature of formation as determined from the clumped isotopic analysis (~40–50 °C) valid?

As can be observed in the burial history of the Hildasay interval, after the initial deposition in a paralic environment the Balder Formation transgression resulted in the interval being buried under marine sediments. It is likely that during this transgressive phase any porewaters in the Hildasay would have been replaced by marine sourced porewaters. Subsequent deposition was dominated by marine sediments culminating in basin-floor fans at the end of the Eocene. Consequently, in the vicinity of the Cambo Field there are no obvious signs of any terrestrial sediments that would have acted as a source of meteoric water that could have entered the reservoir, resulting in the isotopic signature observed in the calcite. A British Geological Survey borehole (99/3) located approximately 50 km to the south of the Cambo Field gives some insight into a possible mechanism by which meteoric porewaters could have been introduced into the Hildasay interval after burial (Stoker et al., 2013). The borehole was located on the Judd high and cored and retrieved Lower Eocene coastal to shallow-marine sediments, overlain by Middle Eocene marine shelf deposits and Upper Eocene basinal marine deposits. While this sequence records an increasingly marine content as would be expected from the stratigraphy in the Cambo Field area, analysis of the core revealed a transgressive gravel lag at the base of the Middle Eocene. The lag comprised a weathered and iron-stained sequence, interpreted as a subaerially eroded contact with the underlying lower Middle Eocene shallow marine deposits. Stoker et al. (2013) have suggested that the area that was subaerially exposed was laterally extensive and probably included much of the southern end of the Faroe-Shetland Basin. This mid-Lutetian period of sub-aerial exposure may have been the last opportunity for meteoric water to enter the Hildasay reservoir, as subsequent deposition would have been dominated by marine sediments, isolating the Hildasay from any further meteoric influence. Stoker et al. (2013) report that the sediments immediately underneath the mid-Lutetian unconformity comprise coastal and shallow marine deposits that contain abraded shelly

material and that ferroan calcite cementation is present. Consequently, it is possible that these sandstones could have been the source of calcium for the ferroan calcite precipitated in the Hildasay sands. As the sediments present at the unconformity are mid-Ypresian to early Lutetian in age, there would have needed to have been cross-formational flow for the meteoric water to enter the Hildasay sands. A simplified cross section (Fig. 12) based upon the seismic and log data of wells located between the 99/3 borehole and the Cambo Field highlights the potential flow path for meteoric fluids to enter the basin.

If the mid-Lutetian Unconformity is the source of the meteoric porewater that entered the Hildasay and gave rise to the precipitation of the ferroan calcite, the water ingress would have been ~45 Mya, approximately ten million years after the deposition of the Hildasay reservoir. If this were the case and the calcite precipitated soon after the ingress of the meteoric water this would have occurred when the Hildasay would be at a depth of less than 1 km, and at a temperature of ~40 °C (Fig. 11). The clumped isotope analysis supports the model, both with regards a meteoric origin of the fluids, and a temperature of formation from 40 to 50 °C during shallow burial. The outer margins of the cemented interval record the more depleted δ^{18}O values (δ^{18}O$_{PDB}$ = −12.01 and −12.2‰) which may reflect an increase in temperature of formation during burial. There are similarities in the model for the Hildasay calcite cementation and that proposed by Watson et al. (1995), for calcite concretions present in the Balmoral oil field in the Central North Sea. Watson et al. (1995) proposed that concretion growth in the deep water turbidite sandstones of the Palaeocene Andrew Member occurred at burial depths of <500 m, commencing in the zone of methanogenesis and thermocatalytic decarboxylation, with further growth during meteoric flushing. Watson et al. (1995) proposed the source of the meteoric water to be from the East Shetland Platform ~140 km NW of the field. The model proposed for the Hildasay carbonate cementation is similar although there is no evidence of decarboxylation, as the temperature in the reservoir never exceeded 60 °C, and hydrocarbon migration into the Cambo began in the late Eocene/early Oligocene (Gardiner et al. 2019) after the calcite cementation had occurred. Also, the distance between the Hildasay sands and the likely source of meteoric water at the mid-Lutetian unconformity is considerably less (<50 km). The present study has shown the benefit of using clumped isotopes where both the composition of the pore water and the temperature of precipitation can be determined. These data, combined with knowledge of the burial history of the sediments, have given strong support to the proposed model for the formation of the carbonate cementation observed in the Hildasay reservoir sandstones.

6.2. Potential impact on reservoir performance

While concretions will have a negative impact on oil volumes in place but not on fluid flow, laterally extensive (kilometre scale) cemented beds can have a negative impact on both volumes and oil recovery. If their presence is not taken into account when deciding the location of oil production wells and water injectors, sweep efficiency may be severely reduced. If the model proposed is correct then the carbonate-cemented units will be restricted to the fine-grained bioturbated deposits with carbonaceous material, locally deposited within the estuarine channel environment. Given the high energy of the estuarine channels and their potential to erode into the finer grained deposits it is likely that the cemented intervals will have a limited lateral extent. Oil geochemical analysis shows that the carbonate-cemented intervals are not sealing, as oil with the same organic geochemical signature has been sampled both above and below the calcite-cemented interval in the well studied. It is possible that these cemented intervals may act as baffles to flow, consequently reducing the reservoir effective vertical permeability by making the flow paths from the injectors to producers more tortuous and may improve sweep efficiency (Mijnssen et al., 1992; Lien et al., 1992).

7. Conclusions

The early Eocene Hildasay reservoir in the Cambo Field is dominated by high porosity and permeability sandstones deposited in a paralic environment. Locally the sandstones are extensively cemented by ferroan calcite intervals that vary in thickness from decimetre to over 1 m thick that have no effective porosity. Petrographic and isotopic analysis supports a model whereby the cementation is stratabound and
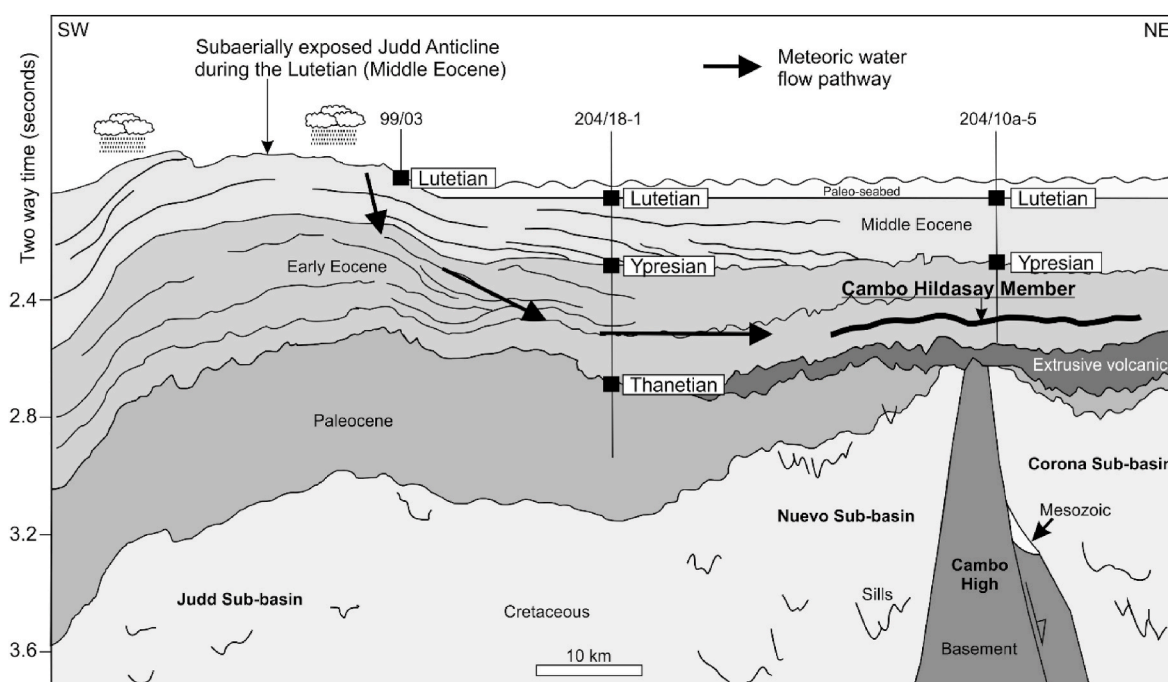

Fig. 12. Geological cross section showing pathway for meteoric water to enter the Hildasay reservoir during the mid-Lutetian unconformity. Model based upon seismic data (flattened on mid-Lutetian unconformity) and well data. Line of section shown in Fig. 1.

linked to thin, finer-grained sandstone deposits containing kerogen, amorphous organic matter and synsedimentary sphaerosiderite. The early siderite in the centre of the cemented interval is replaced by ferroan calcite with a high δ^{13} carbon isotopic signature (δ^{13} $C_{VPDB} = 7.53‰$) suggesting that it formed during anaerobic methanogenesis or fermentation. It is likely that this early phase of ferroan carbonate acted as a nucleus for later ferroan calcite cementation. Subsequent ferroan calcite was precipitated with a lower δ^{13} carbon isotopic signature (δ^{13} $C_{VPDB} = 0.72$ to $-3.68‰$), and the outer margins of the cemented interval have a more depleted δ^{13} carbon signature (δ^{13} $C_{VPDB} = -15‰$) more typical of a strong aerobic oxidation source. Oxygen isotopic analysis supports a meteoric origin for the cements, with clumped isotopes suggesting that the calcite formed at ~40–50 °C, when the reservoir was at a depth of <1 km, from pore waters with a meteoric signature (δ^{18} $O_{VSMOW} = -4.8$ to $-5.7‰$). The source of the meteoric influx was likely to have been related to the subaerial exposure of strata to the south of the Cambo Field during the mid-Lutetian unconformity. The cemented intervals are likely not to be spherical concretions but discrete layers, associated with the finer grained deposits that contain the woody material and early siderite. Given the general high energy environment of the estuarine sands it is likely that these intervals will not be field wide barriers to flow, but more likely to be local baffles.

CRediT authorship contribution statement

Kevin Purvis: Conceptualization, Investigation, Supervision, Writing - original draft. **Paul Dennis:** Conceptualization, Methodology, Validation, Investigation, Resources, Writing - review & editing. **Liam Holt:** Investigation, Writing - original draft, Visualization. **Alina Marca:** Methodology, Validation, Investigation.

Declaration of competing interest

The authors declare that they have no known competing financial interests or personal relationships that could have appeared to influence the work reported in this paper.

Acknowledgements

Appendix B. Supplementary data

Supplementary data to this article can be found online at https://doi.org/10.1016/j.marpetgeo.2020.104641.

APPENDIX A

Techniques

Petrographic analysis – Polished thin sections were analysed for their cathodoluminescence using a Technosyn CL Cold Cathode 8200 mk3 with a digital camera attached. Petrographic analyses were undertaken at Aberdeen University Geology Department.

SEM analysis – Samples were analysed using a Carl Zeiss Sigma VP Field Emission SEM operating at an accelerating voltage of 20 kV in variable pressure mode. Mineral composition was undertaken using Energy Dispersive Spectroscopy (EDS) using a Bruker Quantax 400 Energy Dispersive Spectrometer equipped with an Xflash 5030 Silicon Drift Detector. The EDS detector is equipped with an ultra-thin window allowing detection of elements down to carbon. SEM analysis was undertaken at the James Hutton Institute, Aberdeen.

XRD analysis (Whole Rock) – The bulk samples were wet ground in ethanol in a McCrone mill and spray dried to produce a random powder. The X-ray powder diffraction (XRPD) patterns were recorded from 2 to 75°θ2 using Cobalt Kα radiation. Quantitative analysis was done by a normalised full pattern reference intensity ratio (RIR) method. Expanded uncertainty uses a coverage factor of 2 i.e. 95% confidence is given by$\pm X^{0.35}$ where X = concentration in weight %, e.g. 30 wt% ± 3.3.

XRD analysis (Clay fraction) – Clay fractions of <2 μm were obtained by timed sedimentation, prepared as an orientated mount using the filter peel transfer technique and scanned from 2 to 45°2θ in the air-dried state, after glycolation and after heating to 300 °C for 1 h. Clay minerals identified were quantified using a mineral intensity factor approach based on calculated XRPD patterns. For clay minerals present in amounts >10 wt% uncertainty is estimated as better than ± 5 wt% at the 95% confidence level. All XRD analysis was undertaken at the James Hutton Institute, Aberdeen.

APPENDIX B

Isotope analysis - Technical summary

(i) Sample preparation

Samples were prepared and analysed following the method described in Dennis et al. (2019) with some modifications to the procedure, notably the acid reaction mode and reaction temperature. Samples were carefully crushed and homogenized in an agate pestle and mortar. Approximately 10 mg (equivalent to 4 mg of calcite) of each sample was reacted at 87 °C with 102% ortho-phosphoric acid in a common-acid bath reaction vessel for a period of 30 min. As the reaction proceeded the evolved CO_2 was collected by cryodistilling into a cold finger at -196 °C. Following reaction any non-condensable gases were removed by vacuum pumping the frozen CO_2. The cold finger was then warmed and held at -120 °C, sublimating the CO_2 at low pressure and cryodistilling it into a barocell manometer via a further two glass spiral traps cooled to -116 °C. This ensured that the analyte gas is dried to a very low partial pressure of H_2O. At this step any further non-condensable gas resulting from small leaks or desorption from the glass

vacuum system is pumped away. After measurement of the gas pressure and yield the CO_2 was frozen into a cold finger attached to the mass spectrometer inlet via a Porapak-Q trap (200 mm long x 9 mm diameter) cooled to $-20\,°C$. The transfer time through the Porapak-Q was 30 min and is sufficient to ensure 100% recovery of the CO_2. Whilst still frozen a final stage of removing non-condensable gases is undertaken before warming to room temperature and admitting the gas to the sample inlet side of the mass spectrometer.

(ii) Mass spectrometry

The mass spectrometer procedure follows the exact protocol described in Dennis et al. (2019) with measurement of δ^{45} - δ^{49} on the University of East Anglia MIRA dual-inlet isotope ratio mass spectrometer (Dennis et al., 2014).

The data processing algorithms are described in Dennis et al. (2019) and a copy of the Mathematica program used for calculating δ and Δ values from the mass spectrometer data is included in the supplementary information, together with an example of the mass spectrometer raw data output.

It is important to note that the MIRA mass spectrometer is completely linear with respect to the calculated Δ_{47} and Δ_{48} of samples as a function of their bulk isotopic composition as represented by δ^{47} ($\delta^{47} \approx \delta^{13}C + \delta^{18}O$) and δ^{48} ($\delta^{48} \approx 2 \times \delta^{18}O$) over a range of $\delta > 65‰$ (Dennis, 2014). Thus, there are no Pressure Base Line (PBL) effects (Bernasconi et al., 2013) or other non-linearity effects (Huntington et al., 2009) that need to be corrected for.

To ensure a robust calibration of scale compression and transfer function between the local reference frame for Δ_{47} and the absolute reference frame (ARF) we now use the carbonate standards ETH1, ETH3 and ueacmst (UEA Carrara marble) (Bernasconi et al., 2018) with the following Δ_{47} values for CO2 prepared from the standards using the procedure outlined above (i.e. at a reaction temperature of 87 °C): ETH1 = 0.218‰, ETH3 = 0.613‰ and ueacmst = 0.322‰. These values were determined by us in the UEA laboratory calibrating against a scale prepared using 1000 °C heated and 20 °C water equilibrated gases rather than the values suggested by Bernasconi et al. (2018).

Finally, in order to bring our measured results in line with those for samples reacted offline at 25 °C we make a final correction for the difference in the Δ_{47} acid fractionation factor between 25 °C and 87 °C. Using a range of carbonates with different bulk and clumped isotope compositions we have measured a 0.062‰ difference between acid fractionation factors for off-line reaction at 25 °C and on-line reaction in a common acid bath at 87 °C. This empirical value agrees well with the theoretical value calculated by Guo et al. (2009). To avoid any ambiguity when reporting Δ_{47} we only report values after having been corrected to a notional reaction at 25 °C.

(iii) Temperature calibration

For this study we have used the temperature calibration determined at UEA using biogenic carbonates (bivalves and foraminifera) and travertine samples collected from sites with well-characterized temperatures (Kirk, 2017) and prepared and analysed under conditions that can directly be related to the analysis of samples from this study:

$$\Delta_{47} = \frac{3.890(\pm 0.0025) \times 10^4}{T^2} + 0.2139(\pm 0.0280)$$

where T is absolute temperature. The calibration was made over the temperature range 0 °C–56 °C and covers the temperature of samples we report here. We note that this calibration is within measurement uncertainty in agreement with recent calibrations of Petrizzo et al. (2014), Kluge et al. (2015) and Kelson et al. (2017) and lies very close to the theoretical estimates of the temperature dependence of heavy isotope clumping in CO_2 analyte gas produced by reaction of calcite with ortho-phosphoric acid at 25 °C (Schauble et al., 2006; Guo et al., 2009). Extrapolating our calibration to 873 K (the recrystallisation temperature of ETH1) we project a Δ_{47} of 0.265 which is close to our measured value of 0.280. We consider that these observations indicate that the UEA calibration is robust over the range of temperatures encountered in this study. For a more complete discussion of the UEA temperature calibration and how it relates to other studies see Dennis et al. (2019).

(iv) Fluid oxygen isotope composition

To estimate the pore fluid isotope composition at the time of precipitation we have used the experimental determination of the fractionation factor for ^{18}O exchange between calcite and water of Kim and O'Neil (1997).

$$1000ln\alpha = \frac{18.039(\pm 0.365) \times 10^3}{T} - 32.42(\pm 1.2196)$$

We have determined the $\pm 1\sigma$ errors of the calibration by replotting the original data of Kim and O'Neil (1997).

(v) Data quality and contamination

The Δ_{47} reported in Table 4 and the supplementary data are for samples that cover a wide range of δ^{47} (-1‰ to $-25‰$ measured with respect to the mass spectrometer working reference gas, Table 1 of the supplementary material). The calculated Δ_{47} is independent of δ^{47}. Whilst this observation is not an explicit test of non-linearity resulting from contamination the $\delta^{18}O$ of the cements suggest they formed from a fluid with a near constant oxygen isotope composition and over a very limited range of temperatures. In this scenario Δ_{47} should be similar for all samples. That we observe this and that Δ_{47} is also independent of δ^{47} suggests there is not a contaminant in the analyte gases that is isobaric with the m/z = 47 CO_2 isotopologue. Moreover, the Δ_{48} for all the samples is constant with a value of $-0.24‰$ (± 0.017, 1se, n = 21) on the local UEA reference frame. Because the m/z = 48 CO_2 isotopologue is only present at 10% of the m/z = 47 isotopologue it is more sensitive to the presence of contaminants. Were contaminants present we would expect to see significant positive shifts in Δ_{48}. We interpret these two observations as being a strong indication that the Δ_{47} are accurate and robust and that there is no contamination of the analyte gases prepared from these samples despite the fact they are complex mineralogically and contain organic material in the form of woody matter.

The samples, notably C2, also contain siderite. It's not possible to determine how much reaction of siderite with the acid has contributed to the clumped isotope sample analyses. However, Rosenbaum and Sheppard (1986) report that at a reaction temperature of 100 °C the gas yield from siderite ground to $<60\,\mu m$ is $<10\%$ for a 30-min reaction time. Thus, we conclude that whilst the analyte gases may contain a small CO_2 component

resulting from the reaction of siderite the bulk and clumped isotope data are largely representative of the ferroan calcite.

(vi) Data summary

A full data summary is included in the supplementary material. The summary contains the raw δ^{45} - δ^{49}, δ^{13}C and δ^{18}O, and Δ_{47} - Δ_{49} for all samples and standards, calibration plots and transfer functions, and plots of Δ_{47} *versus* δ^{47} and Δ_{48} *versus* δ^{48}.

References

Bjorkum, P.A., Walderhaug, O., 1993. Isotopic composition of a calcite-cemented layer in the Lower Jurassic Bridport Sands, Southern England: implications for formation of laterally extensive calcite-cemented layers. J. Sediment. Petrol. Vol. 63 (4), 678–682. https://doi.org/10.1306/D4267BB3-2B26-11D7-8648000102C1865D.

Bristow, T.F., Bonifacie, M., Derkowski, A., Eiler, J.M., Grotzinger, J.P., 2011. A hydrothermal origin for isotopically anomalous cap dolostone cements from south China. Nature 474 (7349), 68–71. https://doi.org/10.1038/nature10096.

Bryant, I.D., Kantorowicz, J.D., Love, C.F., 1988. The origin and recognition of laterally extensive continuous carbonate-cemented horizons in the Upper Lias Sands of southern England. Mar. Petrol. Geol. 5, 108–133. https://doi.org/10.1016/0264-8172(88)90018-9.

Budd, D.A., Hammes, U., Ward, W.B.(, 2000. Cathodoluminescence in calcite cements: new Insights on Pb and Zn sensitizing, Mn activation, and Fe quenching at low trace-element concentrations. J. Sediment. Res. 70 (1), 217–226. https://doi.org/10.1306/2DC4090C-0E47-11D7-8643000102C1865D.

Carvalho, M.V.F., De Ros, L.F., Gomes, N.S., 1995. Carbonate cementation patterns and diagenetic reservoir facies in the Campos Basin Cretaceous turbidites, offshore eastern Brazil. Mar. Petrol. Geol. 12, 741–758. https://doi.org/10.1016/0264-8172(95)93599-Y.

Cohen, K.M., Finney, S.C., Gibbard, P.L., Fan, J.-X., 2013. Updated) the ICS International Chart. Episodes 36, 199–204. https://doi.org/10.18814/epiiugs/2013/v36i3/002.

Coleman, M.L., Raiswell, R., 1981. Carbon, oxygen and sulphur isotope variations in concretions from the Upper Lias of N.E. England. Geochem. Cosmochim. Acta 45, 329–340. https://doi.org/10.1016/0016-7037(81)90243-X.

Coleman, M.L., Raiswell, R., 1993. Microbial mineralization of organic matter: mechanisms of self-organization and inferred rates of precipitation of diagenetic minerals. Philos. Trans. R. Soc. London, Ser. A: Physical and Engineering Sciences 344 (1670), 69–87. https://doi.org/10.1098/rsta.1993.0076.

Deer, W.A., Howie, R.A., Zussman, J., 1962. Rock-Forming Minerals, vol. 5. Non-Silicates. Longmans, London, p. 371. https://doi.org/10.1180/minmag.1963.033.261.16.

Dennis, P.F., Myhill, D.J., Kirk, R., Marca, A., 2019. Clumped isotope evidence for episodic, rapid flow of fluids in a mineralized fault system in the Peak District, UK. J. Geol. Soc. 176 (3), 447–461. https://doi.org/10.6084/m9.figshare.3808329.v9.

Dutton, S.P., 2008. Calcite cement in Permian deep-water sandstones, Delaware Basin, west Texas: origin, distribution, and effect on reservoir properties. AAPG Bull. 92, 765–787. https://doi.org/10.1306/01280807107.

Eiler, J.M., 2007. "Clumped-isotope" geochemistry—the study of naturally-occurring, multiply-substituted isotopologues. Earth Planet Sci. Lett. 262, 309–327. https://doi.org/10.1016/j.epsl.2007.08.020.

Fielding, K.D., Burnett, D., Crabtree, N.J., Ladegaard, H., Lawton, L.C., 2014. – Exploration and appraisal of a 120km2 four-way dip closure: what could possibly go wrong? From Cannon. In: C, S.J., Ellis, D. (Eds.), Hydrocarbon Exploration to Exploitation West of Shetlands, vol. 397. Geological Society, London, Special Publication, pp. 145–162. https://doi.org/10.1144/sp397.11.

Gardiner, D., Schofield, N., Finlay, A., Mark, N., Grove, C., Forster, C., Moore, J., 2019. Modeling petroleum expulsion in sedimentary basins: the importance of igneous intrusion timing and basement composition. Geology 47 (10), 904–908. https://doi.org/10.1130/g46578.1.

Huntington, K.W., Lechler, A.R., 2015. Carbonate clumped isotope thermometry in continental tectonics. Tectonophysics 647–648, 1–20. https://doi.org/10.1016/j.tecto.2015.02.019.

Irwin, H., Curtis, C., Coleman, M., 1977. Isotopic evidence for source of diagenetic carbonates formed during burial of organic-rich sediments. Nature 269 (5625), 209–213. https://doi.org/10.1038/269209a0.

Jolley, D., 2012. Biostratigraphy and ecology of early Eocene Flett, balder and horda formations in the Cambo area, corona ridge, Faroe-Shetland Basin. Internal company report.

Lanson, B., Beaufort, D., Berger, G., Bauer, A., Cassagnabere, A., Meunier, A., 2002. Authigenic kaolin and illitic minerals during burial diagenesis of sandstones: a review. Clay Miner. 37, 1–22. https://doi.org/10.1180/0009855023710014.

Lien, S.C., Haldorsen, H.H., Manner, M., 1992. Horizontal wells: still appealing in formations with discontinuous vertical permeability barriers? J. Petrol. Technol. 1364–1370. https://doi.org/10.2118/20962-pa.

Loyd, S.J., Dickson, J.A.D., Boles, J.R., Tripati, A.K., 2014. Clumped-isotope constraints on cement paragenesis in septarian concretions. SEPM Journal of Sedimentary Research 84 (12), 1170–1184. https://doi.org/10.2110/jsr.2014.91.

Ludvigson, G.A., Gonzalez, L.A., Metzger, R.A., Witzke, B.J., Brenner, R.L., Murillo, A.P., White, T.S., 1998. Meteoric sphaerosiderite lines and their use for paleohydrology and paleoclimatology. Geology 26 (11), 1039–1042. https://doi.org/10.1130/0091-7613(1998)026<1039:mslatu>2.3.co;2.

Luetkemeyer, P.B., Kirschner, D.L., Huntington, K.W., Chester, J.S., Chester, F.M., Evans, J.P., 2016. Constraints on paleofluid sources using the clumped-isotope

thermometry of carbonate veins from the SAFOD (San Andreas Fault Observatory at Depth) borehole. Tectonophysics 690, 174–189. https://doi.org/10.1016/j.tecto.2016.05.024.

McBride, E.F., 1963. A classification of common sandstones. J. Sediment. Petrol. 33, 664–669. https://doi.org/10.1306/74d70ee8-2b21-11d7-8648000102c1865d.

McInerney, F.A., Wing, S.L., 2011. The Paleocene-eocene thermal maximum: a perturbation of carbon cycle, climate, and biosphere with implications for the future. Annu. Rev. Earth Planet Sci. 39, 489–516. https://doi.org/10.1146/annurev-earth-040610-133431.

Mijnssen, F.C.J., Weber, K.J., Rozendal, S., Kool, H., 1992. The effect of horizontal shales on vertical permeability in clastic reservoir rocks. In: Spencer, A.M. (Ed.), Generation, Accumulation and Production of Europe's Hydrocarbons II. Springer-Verlag, Berlin Heidelberg, pp. p279–289. Special Publication of the European Association of Petroleum Geoscientists No. 2.

Moore, S.E., Ferrell JR., R.E., Aharon, P., 1992. Diagenetic siderite and other ferroan carbonates in a modern subsiding marsh sequence. J. Sediment. Petrol. 62 (3), 327–366. https://doi.org/10.1306/d4267901-2b26-11d7-8648000102c1865d.

O'Neil, J.R., 1987. Preservation of H, C and O isotopic ratios in the low temperature environment. In: Kyser, T.K. (Ed.), Stable Isotope Geochemistry of Low Temperature Fluids, pp. 85–128. Min. Assoc. of Canada Short Course 13.

Picard, A., Gartman, A., Clarke, D.R., Girguis, P.R., 2018. Sulfate-reducing bacteria influence the nucleation and growth of mackinawite and greigite. Geochem. Cosmochim. Acta 220, 367–384. https://doi.org/10.1016/j.gca.2017.10.006.

Pye, K., Dickson, J.A.D., Schiavon, N., Coleman, M.L., Cox, M., 1990. Formation of siderite-Mg-calcite-iron sulphide concretions in intertidal marsh and sandflat sediments, north Norfolk, England. Sedimentology 37, 325–343. https://doi.org/10.1002/9781444304459.ch2.

Schauble, E.A., Ghosh, P., Eiler, J.M., 2006. Preferential formation of ^{13}C–^{18}O bonds in carbonate minerals, estimated using first-principles lattice dynamics. Geochem. Cosmochim. Acta 70 (10), 2510–2529. https://doi.org/10.1016/j.gca.2006.02.011.

Schmitz, B., Pujalte, V., 2007. Abrupt increase in seasonal extreme precipitation at the Palaeocene-Eocene boundary. Geology 35, 215–218. https://doi.org/10.1130/g23261a.1.

Stoker, M.S., Leslie, A.B., Smith, K., 2013. A record of Eocene (Stronsay Group) sedimentation in BGS borehole 99/3, offshore NW Britain: implications for early post-break-up development of the Faroe-Shetland Basin. Scot. J. Geol. v49, 133–148. https://doi.org/10.1144/sjg2013-001.

Trefrey, J.H., Presley, B.J., 1982. Manganese fluxes from Mississippi Delta sediments. Geochimica et Cosmochimica Acta, v 46, 1715–1726. https://doi.org/10.1016/0016-7037(82)90112-0.

Veillard, C.M.A., John, C.M., Krevor, S., Najorka, J., 2019. Rock-buffered recrystallization of Marion Plateau dolomites at low temperature evidenced by clumped isotope thermometry and X-ray diffraction analysis. Geochem. Cosmochim. Acta 252, 190–212. https://doi.org/10.1016/j.gca.2019.02.012.

Walderhaug, O., Bjorkum, P.A., Nordgard Bolas, H.M., 1989. Correlation of calcite-cemented layers in shallow marine sandstones of the Fensfjord Formation in the Brage Field. In: Collinson, J.D. (Ed.), Correlation in Hydrocarbon Exploration. Graham and Trotman, London, pp. 367–375. https://doi.org/10.1007/978-94-009-1149-9_28.

Watson, R.S., Trewin, N.H., Fallick, A.E., 1995. The formation of carbonate cements in the Forth and Balmoral Fields, northern North Sea: a case of biodegradation, carbonate cementation and oil leakage during early burial. In: Hartley, A.J., Prosser, D.J. (Eds.), Characterisation of Deep Marine Clastic Systems. Geological Society Special Publication No. 94, pp. 177–200. https://doi.org/10.1144/gsl.sp.1995.094.01.13.

Wilkinson, M., 1992. Reply to discussion on the concretions of the bearrerraig sandstone formation: geometry and geochemistry. Sedimentology 39, 517–520. https://doi.org/10.1111/j.1365-3091.1992.tb02133.x.

References

Bernasconi, S.M., Hu, B., Wacker, U., Fiebig, J., Breitenbach, S.F.M., Rutz, T., 2013. Background effects on Faraday collectors in gas-source mass spectrometry and implications for clumped isotope measurements. Rapid Commun. Mass Spectrom. 27 (5), 603–612. https://doi.org/10.1002/rcm.6490.

Bernasconi, S.M., Müller, I.A., Bergmann, K.D., Breitenbach, S.F.M., Fernandez, A., Hodell, D.A., et al., 2018. Reducing uncertainties in carbonate clumped isotope analysis through consistent carbonate-based standardization. G-cubed 72 (22). https://doi.org/10.1029/2017GC007385, 5351–20.

Dennis, Paul, 2014. On the cause of mass spectrometer non-linearity during clumped isotope measurements. figshare. https://doi.org/10.6084/m9.figshare.1254807.v1.

Dennis, Paul F., Vinen, S., Marca-Bell, A., Rowe, P.J., 2014. MIRA: a new isotope ratio mass spectrometer for clumped isotope studies of CO_2. figshare. https://doi.org/10.6084/m9.figshare.899817.v1.

Guo, W., Mosenfelder, J.L., Goddard III, W.A., Eiler, J.M., 2009. Isotopic fractionations associated with phosphoric acid digestion of carbonate minerals: insights from first-principles theoretical modeling and clumped isotope measurements. Geochem. Cosmochim. Acta 73 (24), 7203–7225. https://doi.org/10.1016/j.gca.2009.05.071.

Huntington, K.W., Eiler, J.M., Affek, H.P., Guo, W., Bonifacie, M., Yeung, L.Y., et al., 2009. Methods and limitations of "clumped" CO_2 isotope (Δ_{47}) analysis by gas-source isotope ratio mass spectrometry. J. Mass Spectrom. 44 (9), 1318–1329. https://doi.org/10.1002/jms.1614.

Kelson, J.R., Huntington, K.W., Schauer, A.J., Saenger, C., Lechler, A.R., 2017. Toward a universal carbonate clumped isotope calibration: diverse synthesis and preparatory methods suggest a single temperature relationship. Geochem. Cosmochim. Acta 197, 104–131. https://doi.org/10.1016/j.gca.2016.10.010.

Kim, S.-T., O'Neil, J.R., 1997. Equilibrium and nonequilibrium oxygen isotope effects in synthetic carbonates. Geochem. Cosmochim. Acta 61 (16), 3461–3475. https://doi.org/10.1016/S0016-7037(97)00169-5.

Kirk, R., 2017. Development of Clumped Isotope Techniques and Their Application to Palaeoclimate Studies. University of East Anglia, Norwich. PhD thesis. https://ueaprints.uea.ac.uk/id/eprint/63690.

Kluge, T., John, C.M., Jourdan, A.-L., Davis, S., Crawshaw, J., 2015. Laboratory calibration of the calcium carbonate clumped isotope thermometer in the 25–250 °C temperature range. Geochem. Cosmochim. Acta 157, 213–227. https://doi.org/10.1016/j.gca.2015.02.028.

Petrizzo, D.A., Young, E.D., Runnegar, B.N., 2014. Implications of high-precision measurements of (^{13}C-^{18}O bond ordering in CO2 for thermometry in modern bivalved mollusc shells. Geochem. Cosmochim. Acta 142 (C), 400–410. https://doi.org/10.1016/j.gca.2014.07.017.

Rosenbaum, J., Sheppard, S.M.F., 1986. An isotopic study of siderites, dolomites and ankerites at high temperatures. Geochem. Cosmochim. Acta 50 (6), 1147–1150. https://doi.org/10.1016/0016-7037(86)90396-0.